NTNU

Norwegian University of
Science and Technology

Acquisition, Processing and Interpretation of Geophysical Data from the Fen Complex in Telemark, Norway

Pauline Frydenlund

Petroleum Geoscience and Engineering
Submission date: June 2017
Supervisor: Jan Steinar Rønning, IGP
Co-supervisor: Georgios Tassis, Geological Survey of Norway

Norwegian University of Science and Technology
Department of Geoscience and Petroleum

Preface

This Master's thesis marks the completion of a five-year engineering degree at the Norwegian University of Science and Technology within the field of geophysics. The thesis is written in cooperation with the Geological Survey of Norway and is a continuation of the specialization project written the fall of 2016.

I would like to thank the Geological Survey of Norway and Sven Dahlgren for including me in their joint project at the Fen Complex. A special thank to Jan Steinar Rønning for introducing me to the world of applied geophysics and supervising my work. Co-supervisor and Rayfract® specialist Georgios Tassis, from NGU, deserves a big thanks for teaching me the software skills I needed to complete the work. I would also like to thank Bjørn Eskil Larsen for helping with GIS software and letting me use his office, and Jan Fredrik Tønnesen for providing me with his traditional interpretation of the refraction seismic.

I would like to thank the department of Geophysics at the Geological Survey of Norway for making me feel incredible welcome in the Geological Survey Office and making the fieldwork at the Fen Complex an enjoyable trip and excellent learning experience.

Last, but not least I would like to thank my fellow students at the Department of Petroleum Engineering and Applied Geophysics for their moral support and interesting discussions regarding geophysics, the process of writing a thesis and for a wonderful student experience.

Trondheim, 09.06.2017

Pauline Frydenlund

Abstract

This Master's thesis focuses on the acquisition and processing of geophysical data to map the geology of the Fen Complex in Telemark, Norway. Three resistivity and two seismic profiles where acquired at the Fen Complex during September and October of 2016. The refraction seismic has been processed using traditional techniques, such as Hagedoorn's method, and tomographic inversion using the Rayfract® software. The results from both processing methods have been compared to investigate which method creates the most accurate image of the subsurface. The resistivity has been processed using the RES2DINV software.

The tomographic inversion has been run using different parameters, and a recommendation of the best settings for this study is presented. The results of the resistivity measurements and seismic surveys have been compared to each other and correlated to data from boreholes in close proximity to investigate soil characteristics, depth to bedrock, possible fracture zones and to create a geological interpretation of the area.

The correlation between the depth to bedrock interpreted from the seismic and the resistivity measurements is concluded to be good. As a result, the resistivity measurements can be used to infer the depth to the bedrock. Multiple low velocity zones have been mapped along the seismic profiles and a geological interpretation is presented. The soil characteristics of the area have multiple interpretations. Therefore, further geotechnical investigation is necessary to make a conclusive characterization.

Sammendrag

Denne masteroppgaven omhandler innhentingen og prosesseringen av geofysiske data for å kartlegge geologien på Fensfeltet i Telemark, Norge. Tre linjer med resistivitets målinger og to seismiske profiler ble innhentet på Fen i slutten av september og starten av oktober 2016. Seismikken har blitt tolket med tradisjonelle tolkningsmetoder som Hagedoorns metode og med tomografisk inversjon ved hjelp av Rayfract® programvaren. Resultatene fra prosesseringene er sammenlignet for å vurdere hvilken metode som skaper de mest korrekte modellene av undergrunnen. Resistivitetsmålingene er prosessert med programvaren RES2DINV.

De tomografiske inversjonene har blitt kjørt med forskjellige parametere, og en anbefaling for de beste innstillingene for denne studien er fremlagt. Resultatene fra seismikken og resistivitetsmålingene er sammenlignet med hverandre og med informasjon fra nærliggende borehull for å kunne karakterisere løsmasser, dybde til fjell, mulige svakhetssoner og for å lage en geologisk tolkning av området.

Resultatene fra studien viser svært god sammenheng mellom dybde til fjell tolket fra seismikk og fra resistivitet. Derfor kan resistivitetsdataen benyttes for å indikere dyp til fjell i denne studien. Flere lavhastighetssoner har blitt kartlagt ut ifra de seismiske tolkningene og en geologisk tolkning av området er presentert. Løsmassene i området har sprikende tolkninger. For å komme med en endelig karakterisering er det behov for ytterligere geotekniske undersøkelser.

Table of Contents

List of Figures

List of Tables

1. Introduction

This Master's thesis describes how tomographic inversion, performed with the use of Rayfract® software, can be used to invert seismic information into velocity models. In order to use the software to create tomographic inversions, a start model must be present. The start model can be created by manual interpretation or generated by the software. Models created by manual interpretation based on Hagedoorn's Plus-Minus method, software generated Plus-Minus, wavefront and 1D- Gradient start models have been inverted using Rayfract®. The thesis describes how resistivity measurements can be performed and processed, and how resistivity measurements can be used to classify soil and rocks.

The inverted velocity models generated along with traditional interpretations, resistivity measurements and borehole information are used to decide the depth to the soil-bedrock interface and to locate weakness zones in the bedrock. On the basis of the information provided, a geological interpretation of the area is presented. The thesis is completed in cooperation with the Geological Survey of Norway and Regional Head Geologist of Telemark, Buskerud and Vestfold, Sven Dahlgren, as a part of a project to map the geology of the Fen Complex.

1.1. Background information

The Fen Complex is located in Nome municipality in Telemark, Norway. It is a 5km^2 area with an interesting geological composition (Bryhni and Askheim, 2016). In 1921 the Nowegian geologist W.C. Brøgger studied the area, and claimed that the Fen Complex was an eroded carbonate volcano. Brøggers theory was doubted until the 1960s, when an English geologist witnessed the Oldoinyo Lengai volcano in Tanzania erupting carbonate lavas (Ramberg et al., 2006).

During his studies of the Fen Complex, Brøgger found rocks that previously had not been studied anywhere else in the world. He classified the rocks as carbonatites, and assigned names to the rocks according to the location of discovery. The names

Brøgger assigned are still used for carbonatites all over the world. The present day Fen Complex is reduced to a fraction of the original volcano (Ramberg et al., 2006).

The Master's thesis is a part of the collaboration between the head regional geologist of Telemark, Vestfold and Buskerud, Sven Dahlgren and NGU. The data processed was acquired at the Fen Complex in Telemark between September 29th and October 8th 2016. Three lines of resistivity measurements and two seismic profiles were gathered. During the project there has also been drilled boreholes to map the depth to bedrock in different areas and to classify the bedrock, the data acquired is presented in the thesis.

1.2. Purpose

The purpose of this Master's thesis is to investigate the difference between traditional seismic interpretation and seismic tomography using the Rayfract® software. The thesis will also use resistivity measurements gathered at the Fen Complex and information from boreholes to decide the depth of the soil bedrock boundary and to create a geological interpretation of the area surrounding the investigated profiles.

1.3. Methods used

In this thesis, resistivity measurements and refraction seismic has been used to investigate the subsurface of the Fen Complex. The resistivity measurements were collected with ABEM Terrameter LS and 5 m electrode spacing and processed using the RES2DINVx64 software. The refraction seismic was acquired using dynamite as a source and with 24 geophones along two receiver spreads. The seismic was processed using traditional interpretation techniques and tomographic inversion using Rayfract® software. In addition to the resistivity measurements and the refraction seismic, information from the boreholes located in close proximity to the studied profiles have been consulted to determine the depth to the soil bedrock layer.

1.4. Limitations

The data acquisition was preformed predominantly on fields used for agriculture, the famers tending to the fields had some restrictions to where they would allow dynamite to be fired due to damage to the crops. This affected some of the seismic sections. The

local infrastructure, essentially old unmapped water pipes, made explosions in some shot positions too risky to fire repeatedly.

The planed seismic survey had shots for every 6th geophone, making the distance between shots 30 m. This is at the limit for the minimum recommended geophone to shot ratio when using the Rayfract® software (Rohdewald, 2016). Due to the scarce shot positioning, some sections are unsuited for the wavefront modeling and the result carries evidence of being flawed.

The local infrastructure has also had an effect on the resistivity measurements. Since Fen is an inhabited area there is buried infrastructure, providing households with internet and sanitary facilities. These pipes and wires contain metal that can interfere with the current deployed into the earth and create anomalies in the results.

1.5 Structure of the thesis

The thesis is divided into chapters.

Chapter 2 contains background theory regarding the methods used in the thesis. The theory is focused on basic seismic, refraction seismic, resistivity and how to use the Rayfract® software.

Chapter 3 is a methodical chapter, which explains the work done in the thesis and the measurements and processing performed. The locations of the boreholes are also presented in this chapter.

The results are presented in chapter 4.

Chapter 5 discuses and compares the result of the seismic survey and resistivity measurements to each other and to boreholes and a geological interpretation is presented.

In chapter 6 there are recommendations regarding further work and the conclusion of the thesis is in chapter 7.

2. Theory

In this section the theory behind resistivity measurements, seismic surveys, refraction seismic, tomographic inversion and the RES2DINV and Rayfract® Software will be presented.

2.1 Resistivity measurements

Resistivity measurements also referred to as electrical resistivity tomography, ERT, dates back to the early 1900s. Along with the increase in computers and computer computation power in the 1980s resistivity measurements became more widely used. Resistivity measurements can be used to search for suitable groundwater resources, monitoring groundwater pollution, locate subsurface cavities, faults and fissures, amongst many other applications (Reynolds, 2011). User-friendly inversion software, like RES2DINV, and automated data acquisition systems combined with the method's ability to produce efficient and effective images of the subsurface has contributed to the increased popularity of the method (Dahlin and Zhou, 2006, Dahlin, 1993).

When conducting resistivity measurements a current is employed into the ground thorough a pair of electrodes and another set of electrodes records the potential. The potential and the current are measured at all the electrodes in the configuration to determine an apparent resistivity of the subsurface. The resistivity is defined as ρ [Ωm] (Telford et al., 1990).

2.1.1 Electrode arrays

The most commonly used electrode arrays are the Wenner, the Schlumberger and the dipole-dipole array. The three main arrays have subtypes and all arrays have advantages, disadvantages and sensitivities to take into account when choosing a set-up for a survey (Reynolds, 2011). In the three electrode configurations the placement of the potential and current electrode can be switched without affecting the apparent resistivity, due to the principle of reciprocity (Telford et al., 1990). To achieve the best result, the array for a survey should be based on the desired sensitivity to horizontal and vertical changes in the subsurface (Loke, 1996). According to Dahlin

and Zhou (2004) the basic spacing and the maximum separation of electrodes in an array have direct influence on the spatial resolution and the penetration depth.

The different electrode configuration will lead to different geometric factors, K [m]. Reynolds (2011) defines the geometric factor, K, as shown in equation 1.

$$K = 2\pi\left[\frac{1}{AM} - \frac{1}{MB} - \frac{1}{AN} + \frac{1}{NB}\right]^{-1} \quad (1)$$

AM, MB, AN and NB in equation 1 represents the distances between electrodes. In a homogenous earth the current will flow away radially and the resistivity will be a true value. The earth is not a homogeneous medium and therefore all measured resistivity must be treated as apparent resistivity, ρ_a, not true resistivity. Apparent resistivity is not a physical property of the subsurface and can be negative (Reynolds, 2011).

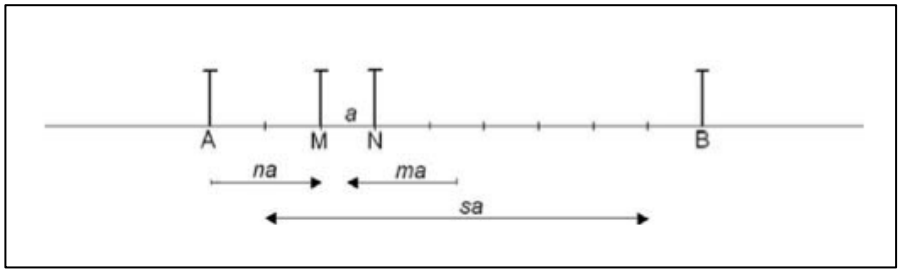

Figure 1: A sketch of the multi-gradient array. Electrodes are placed along the cable and the automatic measuring station sends out currents and measures potential in multiple location, one after one another (Dahlin and Zhou, 2006).

In this project the multi-gradient electrode array, developed by Dahlin and Zhou, was used (Dahlin and Zhou, 2006). The electrode configuration of the array is illustrated in Figure 1. In this study, electrodes are placed with 5 m spacing along the cable. The multi-electrode gradient array differs from the traditional gradient survey because it measures through the electrode layout with a large number of current electrode combinations. When the potential electrodes are placed in the middle of the current electrodes the array will be equal to the Schlumberger array, and when the potential dipole is close to one of the current electrodes it can be considered a pole-dipole array. Due to the difference in array similarities when the potential dipole is moved, the multi-gradient array can be expected to combine characteristics from the various arrays (Dahlin and Zhou, 2006).

2.1.2. Pseudosection

As resistivity data is collected the mid-point between sets of electrodes is plotted along the horizontal axis. On the vertical axis the points are plotted at a distance that is proportional to the separation between the electrodes (Loke, 1996). This way of plotting causes the vertical axis to represent the distance between the electrodes (Dahlin, 1993). The method of plotting is theoretical, which implies that the depth of plotted value is not equal to true depth (Loke, 1996). This plotting is used to create a pseudosection, a linear interpolation between the apparent resistivity values. Using linear interpolation between the points involve no smoothing of the data, which gives a good indication of the data quality (Dahlin, 1993). The pseudosection is displayed on the measuring device in the field, which makes it possible to detect and correct systematic errors while measuring (Dahlin and Zhou, 2006).

2.1.3. Inversion

By inverting the pseudosection a model that could describe the subsurface is created. In this study the inversion software used was RES2DINVx64 version 4.03.25 developed by Geotomo Software. RES2DINVx64 is Windows based software that automatically determines a two-dimensional (2-D) resistivity model from data obtained from electrical imaging surveys (Loke, 1996).

Before letting the program invert the data it is important to make sure that all the data points are representative. In general there are two types of 'bad data points', random and systematic noise (Loke, 1996). Failure during the survey such as bad ground contact, breaks in the cable, connecting the cable in the wrong direction or forgetting to attach electrodes will cause systematic noise. Random noise includes the factors from telluric currents. The effects of telluric currents will be larger at surveys with a larger geometric factor (Loke, 1996). The noise can be removed by using the 'edit data – exterminate bad data points' function in RES2DINVx64, which lets the user select and delete the points which are considered as noise. The systematic noise will be easier to detect than the random noise. In this step the negative apparent resistivity values should also be removed if they are considered noise. The RES2DINVx64 software is designed to operate efficient and accurate when using the standard parameters, but the user can modify the settings (Loke, 1996).

The program has two main useful options when performing inversions. The 'include smoothing of model resistivity' or 'L_2 norm' creates a standard least-squares smoothness constraint and 'select robust inversion' or 'L_1 norm' creates a robust inversion model constraint (Loke, 1996). The robust inversion changes the model parameters while misfit vectors have the same magnitude. This has proven to be a better model where the bodies are internally homogeneous with sharp boundaries (Loke, 1996). The Smoothing option uses a formulation that will apply smoothness constrain directly on the model resistivity values. The smoothing inversion is appropriate to use where there are smooth variation in the boundaries, for instance to locate the boundary of a chemical plume (Loke, 1996). The software tends to give greater importance to outliers and misfits in the data set when using the 'L_2 norm' compared to the 'L_1 norm' (Dahlin and Zhou, 2004).

Measurements in areas with a substantial difference in topography, must take the topography into account when inverting the data set (Loke, 1996). In RES2DINVx64 there are three different ways to handle topography. Figure 2 presents a visual representation of the different topography settings. In locations with small to moderate topographic variation, the first finite-element method could be sufficient to use. The first finite-element approach shifts all the subsurface nodes the same distance as the surface nodes along the same vertical mesh line, a uniformly distorted grid (Loke, 1996). The second finite-element method reduces the amount the subsurface nodes are shifted exponentially with depth, a damped distorted grid. Using this method, cells in great depth will be less affected by the topography than the nodes close to the surface. According to Loke (1996) the damped method creates a better section than the first finite-element approach, but has the disadvantage that the method is prone to produce unusually thick layers beneath sections where the topography curves upwards. The third method is the inverse Schwartz-Christoffel transformation method (Loke, 1996). This method takes the curvature of the surface topography into account and can for certain cases avoid some of the pitfalls of the second finite-element method. The method produces a model that 'looks' more like the measured section (Loke, 1996).

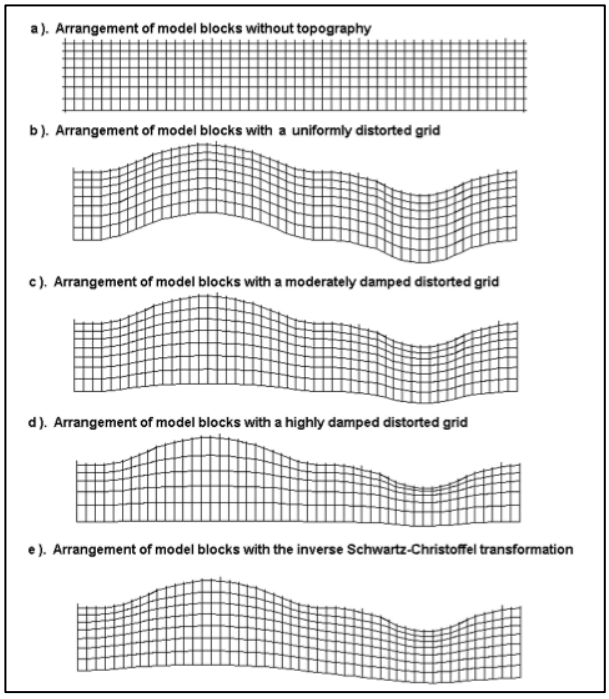

Figure 2: Description of how the grid is change to include topography in the inversion using the different inversion approaches in Res2Dinvx64 (Loke, 2015).

When the inversion is carried out and a section created the absolute error of the section is printed with the profile. When the error is less than 5 % the data and its fit to the model can be considered to be very good, an error in the range of 5-10 % can be considered good. An error between 10-30 % can be considered adequate (Rønning et al., 2017).

2.1.4. Interpretation of model

To interpret the resistivity models NGU has compiled a set of guideline resistivity values in rocks. Table 1 shows how NGU characterizes crystalline rocks based on the resistivity. The values of characterization are wide-ranging with large intervals and high resistivity values.

Table 1: Characterization of weakness zones and rock quality based on resistivity values used by NGU (Rønning et al., 2013).

Resistivity values	Characterization
>3000 Ωm	Good rock quality
3000-500Ωm	Fracture rock and water leakage
<500Ωm	Instable rock mass with clay and water leakage

Soil has much lower resistivity and must be characterized with smaller intervals. Table 2 displays the characterization of soils as tested by Solberg et al. in 2008.

Solberg et al. (2008) determined that quick clay could be determined from resistivity in collaboration with geotechnical tests. The research concluded with the tabulated values presented in Table 2.

Table 2: Tabulated values for characterizing soils based on resistivity (Solberg et al., 2008).

Resistivity values	Characterization
1-10Ωm	Unleached marine clay
10-80 Ωm	Possible quick clay
>80Ωm	Coarser material and bedrock

Based on the two tables with characterizations based on resistivity, it should be possible to locate possible quick clay, soils, fracture zones and possibly faults and depth to bedrock in the data from the Fen Complex.

2.2 Seismic

2.2.1 General Seismic Theory

The principle behind seismic surveys is to monitor waves traveling through the earth from a source whose start time is accurately known (Reynolds, 2011). There are two main types of seismic surveys reflection and refraction seismic. Reflection seismic is one of the main tools used in hydrocarbon exploration. Refraction seismic is used to locate faults, joint and disturbed zones in the subsurface (Reynolds, 2011).

The seismic waves are created from an external force that causes an elastic strain in the material (Reynolds, 2011). There are different kinds if seismic waves. The two main types are surface and body waves. Body waves are the waves that travel though the bulk of a medium, while surface waves are waves that travel along interfaces between medias with contrasts in properties. Body waves are further divided into other categories. P-waves also known as primary, push or compressional waves, oscillate in the direction of travel. S-waves also known as transverse, secondary or shear waves, oscillates perpendicular to the direction of travel (Reynolds, 2011). The velocity of a seismic wave is dependent on the elastic moduli and the densities of the rock they propagate through, and can therefore aid in the interpretation of the type of rock present in the area. Table 3 lists examples of velocities of P-waves in different

materials. As a generalization, velocity increases with increasing density in the rock (Reynolds, 2011).

Table 3: Examples of P-wave velocities from Reynolds (2011).

Material	V_P (m/s)
Air	330
Water	1450-1530
Petroleum	1300-1400
Loess	300-600
Soil	100-500
Snow	350-3000
Solid glacier ice*	3000-4000
Sand (loose)	200-2000
Sand (dry, loose)	200-1000
Sand (water saturated, loose)	1500-2000
Glacial moraine	1500-2700
Sand and gravel (near surface)	400-2300
Sand and gravel (at 2 km depth)	3000-3500
Clay	1000-2500
Estuarine muds/clay	300-1800
Floodplain alluvium	1800-2200
Pemafrost (Quaternary sediments)	1500-4900
Sandstone	1400-4500
Limestone (soft)	1700-4200
Limestone (hard)	2800-7000
Dolomites	2500-6500
Anhydrite	3500-5500
Rock salt	4000-5500
Gypsum	2000-3500
Shales	2000-4100
Granites	4600-6200
Basalts	5500-6500
Gabbro	6400-7000
Peridotite	7800-8400
Serpentinite	5500-6500
Gneiss	3500-7600
Marbles	3780-7000
Sulphide ores	3950-6700
Pulverised fuel ash	600-1000
Made ground (rubble, etc)	160-600
Landfill refuse	400-750
Concrete	3000-3500
Disturbed soil	180-335
Clay landfill cap (compacted)	355-380

*Strongly temperature-dependent for polar ice (Kohnen, 1974).

The Norwegian Geotechnical Institute has tested the relationship between the rock quality data designation, RQD, and P-wave velocities of rocks for shallow refraction surveys (Barton, 2007). The result of the testing is displayed in Figure 3; these results can be used to classify the quality of the bedrock in a refraction seismic survey. The RQD or rock quality designation is an indication of rock quality based on how many

pieces of a core that are longer than 100 mm in relation to the length of the core. Barton (2007) defines RDQ as equation 2.

$$RQD = \frac{sum\ of\ pieces\ \ larger\ than\ 100mm}{total\ length\ of\ core} \times 100\% \quad (2)$$

The model has been tested in several sites and the fits are proven good on shallower sites, depth up to 25 meters (Barton, 2007).

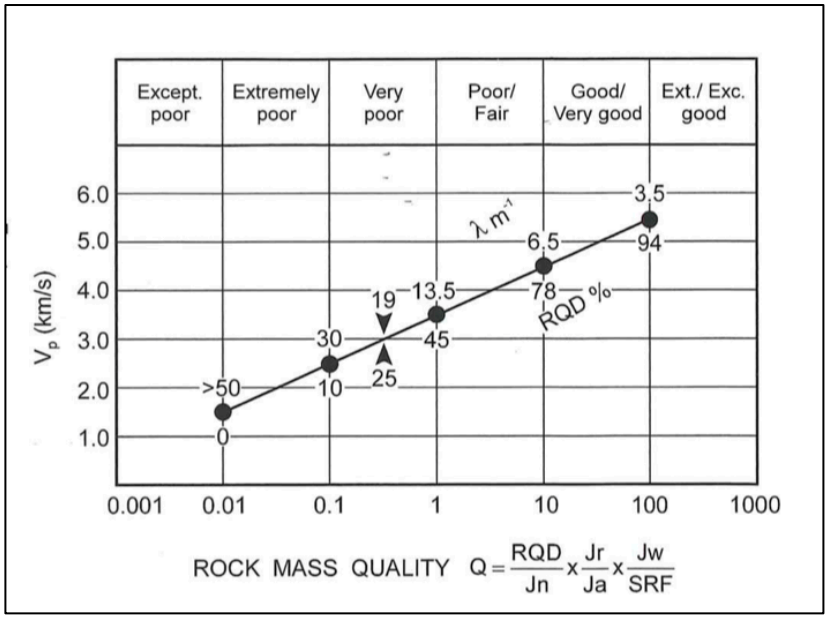

Figure 3: Relationship between rock mass quality and P-wave velocity (Barton, 2007).

The energy source of the seismic survey should be able to exert sufficient energy to generate a measurable signal, have a short duration, have a known shape (or minimal phase) and generate minimal noise (Reynolds, 2011). There are three main groups of energy sources impact, impulse and vibrating sources. Impact sources can be heavy drops or sledgehammers. Impulsive sources uses a detonation, dynamite, or an air or water gun and vibrators are machines that sends out a known vibration (Reynolds, 2011).

The energy emitted from the seismic source is detected by geophones. Each geophone contains a magnet attached to a spring placed inside an electrical coil, which induces an electrical pulse when an acoustic wave propagates at the place of the geophone (Reynolds, 2011). In surveys on water the geophones are replaced with hydrophones that are often towed in streamers (Reynolds, 2011). The geophones or hydrophones are attached to cables that are again attached to a seismograph that records the travel time of the external force and the responses from the geophones (Reynolds, 2011).

2.2.2. Refraction Seismic

The seismic refraction method is based on the fact that seismic waves change the direction of travel upon entry to a new layer with a contrast in parameters. The method is dependent on the velocity increasing with depth, and assumes that the thickness of each layer is greater than the wavelength of the wave in the layer. If these conditions are not met, it may cause a situation known as a hidden layer or velocity inversion. A hidden layer is a layer that is not visible from the data collected through refraction seismic. In refraction seismic the first arrivals of the waves to each geophone contains the interesting information (Reynolds, 2011).

In the refraction seismic survey the data obtained will consist of a set of travel time and distances. These travel times and distances will be used to interpret the depth of the different geological boundaries and velocities in the layers (Nasuti et al., 2010).

From the travel time diagrams the intercept time and crossover point can be extrapolated. The intercept time is found by extending the travel time curve of the second layer to the time axis above the location of the shot. The crossover point is defined as the point where the travel time for the direct and critically refracted waves are equal. A critically refracted wave occurs when the angel of refraction becomes 90°**.** This point can be found by extending the travel time curves for the first and second layer; the point where the lines intersect is the crossover point. The intercept time and the crossover point can be used to calculate the distance to the refractor depth under the geophone using equation 3 and 4 respectively (Reynolds, 2011).

$$z = t_{intercept} \frac{v_1 v_2}{2\sqrt{(v_2^2 - v_1^2)}} \quad (3)$$

$$z = \frac{1}{2} x_{crossover} \sqrt{\frac{v_2 - v_1}{v_2 + v_1}} \quad (4)$$

2.2.3. Hagedoorn's plus-minus method

Hagedoorn's plus-minus method is a method created to interpret refraction seismic data. The method is only valid if it is assumed that the layers are homogeneous, have large velocity contrast and the dip angle of the refractor is less than 10 degrees. If the

assumptions are valid, the accuracy of the depths calculated with Hagedoorn's method should be within a 10 % margin of error (Reynolds, 2011).

Based on the assumptions for Hagedoorn's method, the distance from P to point Q in Figure 4 should be approximately the same distance as the distance x, from S to G. The travel time from S down to A to B and up to G should be equal to the travel time from S to G plus a time delay δt (Reynolds, 2011). The total time delay is equal to the time delay from the shot to point A, plus the time delay from point B to the geophone, known as 'shot-point delay time' and 'geophone delay time' respectively.

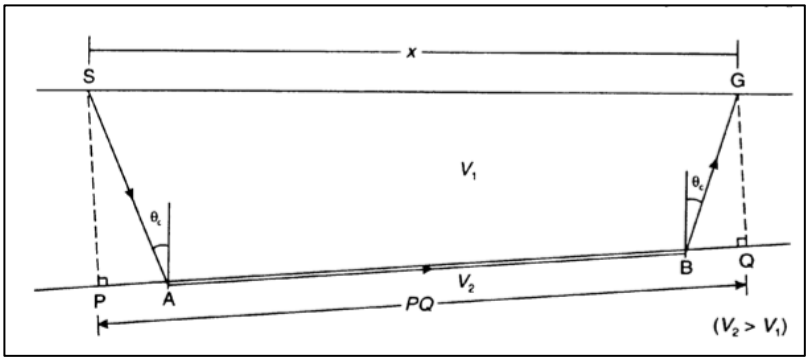

Figure 4: The ray path of seismic wave can be used to calculate the travel time and later the depth of the interface. The image shows the ray path of a forward and a backward shot (Reynolds, 1997).

Using equation 5 from Reynolds (2011), the travel time from a refracted wave can defined with respect to the delay times.

$$T_{SG} = \frac{x}{V_2} + \delta t_{shot} + \delta t_{geophone} \quad (5)$$

A sketch of the ray path of a forward and a reverse shot is shown in Figure 5A. The point G represents a geophone placed in an arbitrary point between a forwards and a backwards shot. Figure 5B shows an example of a travel time versus distance graph. The travel time versus distance graph is used to determine where Hagedoorn's method can be used. The method should only be applied for responses from the same layer (Reynolds, 2011).

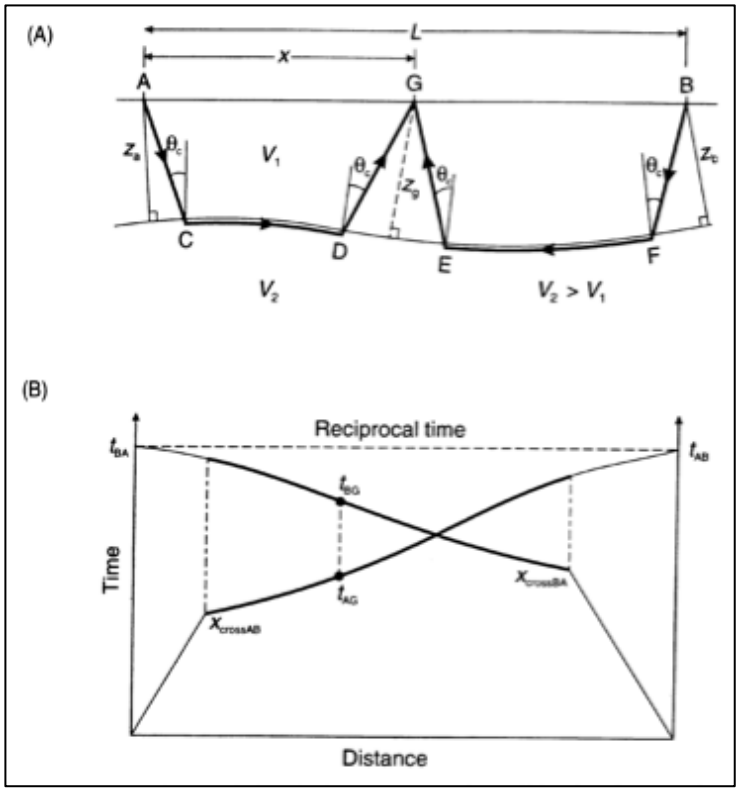

Figure 5: A) A ray path geometry for a forward and a backwards shot from points A and B respectively. Point G is an arbitrary geophone in between. B) Travel time versus distance graph for ray paths from a forward and backward shot (Reynolds, 1997).

Hagedoorn's method consist of one plus and one minus term, the plus term of Hagedoorn's method is the travel times to the geophones added together minus the reciprocal time, equation 6 Reynolds (2011). The plus term is used to find the depth of the interface beneath the geophones. The minus term is the difference in travel time taken by rays form each shot point to a given geophone, equation 7 (Reynolds, 2011).

$$T^{+} = t_{AG} + t_{BG} - t_{AB} \quad (6)$$
$$T^{-} = t_{AG} - t_{GB} \quad (7)$$

Hagedoorn's minus term can be plotted against offset then the velocity can be calculated from the slope. The slope is then equal to $\frac{2}{V_2}$, from which one can derive the velocity in the second layer, V_2. If the slope of Hagedoorn's minus term versus offset has the same slope all over, it can be assumed the velocity in the layer is constant. However if the slope changes, it is an indication that the velocity varies and can indicate a fracture zone. The velocity of layer one can be derived directly from the time-offset plot as $\frac{1}{V_1}$. Once the velocities are calculated the plus term can be used to

calculate the depth of the reflector. Equation 8 shows how the plus term is used together with V_1 and the incidence angle theta to calculate the depth, z, beneath each geophone. The incident angle, θ_c, is defined by Snells law as shown in equation 9 (Reynolds, 2011).

$$z_g = T^+ * \frac{V_1}{2\cos(\theta_c)} \quad (8)$$

$$\sin\theta_c = \frac{v_1}{v_2} \quad (9)$$

In an ideal, homogenous and flat-layered earth the responses from the seismic survey would be straight lines resembling the travel time plot in Figure 5B. The earth is neither homogeneous nor flat; this results in effects on the travel time-distance plots (Reynolds, 2011). Figure 6 shows how different inhomogeneity and changes in topography will affect the travel time versus distance plots. An increase in topography will result in a longer distance from the interface to the geophone and hence a longer travel time, the opposite effect will be present in a reduction in topography. Lenses of sections of material with different velocities will cause the travel time to increase or decrease dependent on the properties of the areas (Reynolds, 2011).

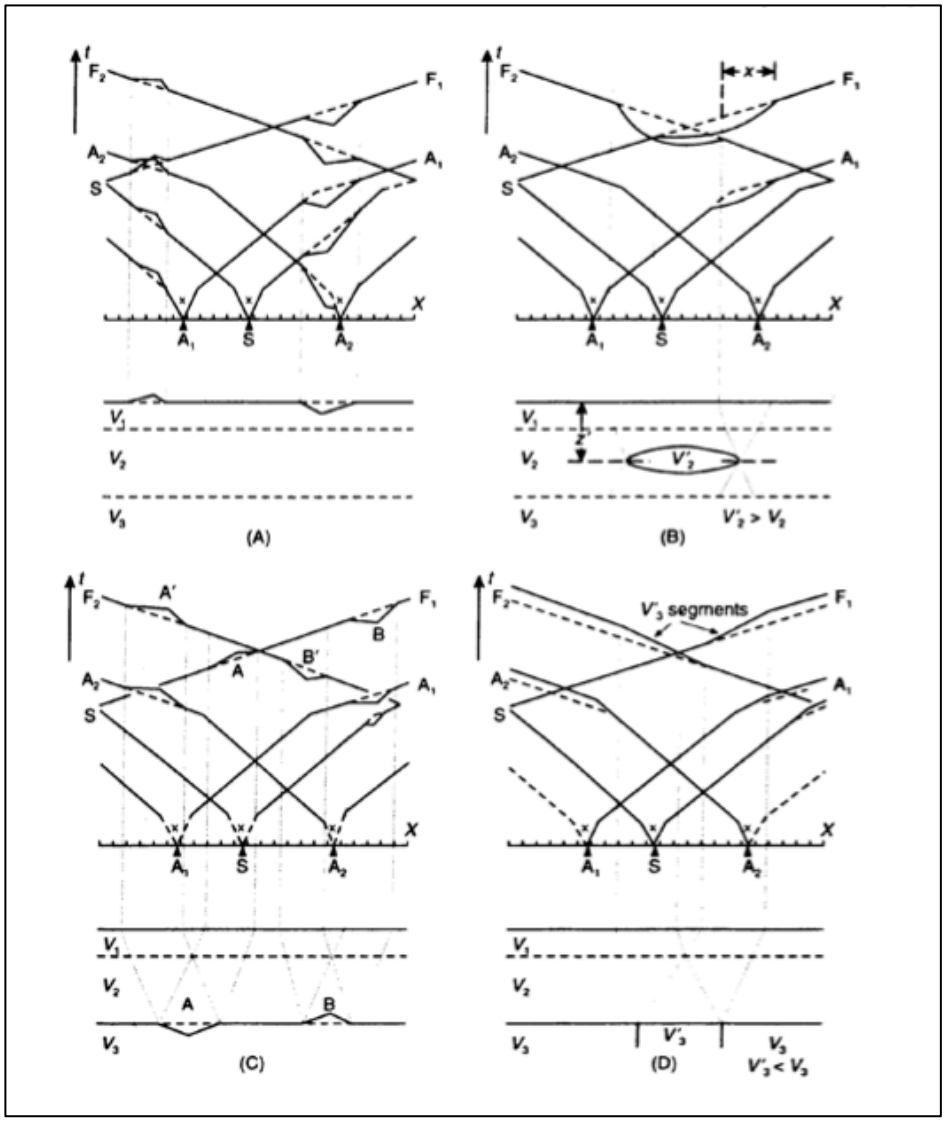

Figure 6: Effects on the travel time versus distance plots of inhomogeneity in the subsurface (Reynolds, 1997).

2.2.4 Seismic Tomography

The method of seismic tomography is relatively new in determining the velocity within the earth. The method has many similarities to the CT or CAT scan method used in hospitals and is different from other earlier methods of calculation the velocity of the earth's materials (Keller, 2000). Based on the data collected during a seismic survey or from an earthquake seismic tomography solves an inverse problem to obtain an heterogeneous seismic model (Rawlinson et al., 2010).

Seismic tomography uses the principle that a body wave traveling through the earth can be expressed by an integral equation (Keller, 2000). When assuming this, one also assumes that the distance divided by the velocity is equal to the travel time of the wave. The plane area between the source and receiver is divided into a grid, where each cell is assigned a velocity. The method sums up the travel time in each cell according to the cells velocity, compares it to the measured velocity. The difference in travel time difference between the calculated and actual travel time, is reduced to a minimum by changing the velocity of the cells iteratively (Reynolds, 2011). The distribution of the ray paths and the number of observations and their accuracy is in direct correlation with the quality of the model, in other words how well the model represents the geology of the area (Keller, 2000). When this method is repeated from different locations, one can use the datasets to locate the area of anomaly (Keller, 2000). As well as calculating the velocity, relative attenuation and Poisson's ratio, which has a great importance for engineering purposes, can be extracted using seismic tomography (Reynolds, 2011).

A common usage of the seismic is between boreholes, known as borehole tomography. The method uses two or more boreholes simultaneously, one hole is used to deploy sources and the other hole(s) contain geophones (Reynolds, 2011).

2.2.5. Eikonal Solvers

By applying the high-frequency approximation of ray theory and searching for plane harmonic solutions to the elastic-wave equations, the Eikonal equations are obtained (Lecomte et al., 2000). The Eikonal equation expressed in two dimensions is

presented in equation 10, where T represents the phase of the solution and s represents the slowness, $\frac{1}{v}$.

$$\left(\frac{\delta T}{\delta x}\right)^2 + \left(\frac{\delta T}{\delta z}\right)^2 = s \quad (10)$$

The Eikonal equations can be solved using multiple different solvers (Kim, 2002). Eikonal solves only requires a velocity or slowness grid and a shot position, and is therefore easy and efficient to use (Vidale, 1988). To create a solution which is robust and accurate for heterogeneous material the slowness in the surrounding structure must be considered (Lecomte et al., 2000).

Lecomte et al. (2000) has created the Eikonal solver which is used in the Rayfract® software. The Eikonal solver presented in their work is robust and accurate (Rohdewald, 2016).

2.3 Rayfract® software

Rayfract® is a seismic refraction and borehole tomography software which creates subsurface seismic velocity models for geotechnical engineering and exploration. The software is suited for processing seismic profiles with low, medium or high coverage and is based on the Wavepath Eikonal Traveltime, WET, inversion method (Rohdewald, 2016). The software is developed by Intelligent Resources Inc. and was first released in 1996. Version 3.35 of the software, released in 2016, was used in this thesis.

The Rayfract® software has three different interpretation methods, common midpoint (CMP) intercept time refraction, Plus-Minus and Wavefront. The CMP intercept time refraction method is based on technique designed by Ruhl (1995) (Rohdewald, 2016). The technique determines the shallow refractor properties by carrying out a common midpoint sorting of traveltimes (Ruhl, 1995). The Plus-Minus is based on Hagedoorn's method, which is presented in section 2.2.3. Due to the fact that the Plus-Minus start model assumes that critically refracted rays emerge vertical from the reflector, the start model has lower lateral resolution than the waverfont start model.

As the overburden thickness increases or the velocity contrasts decreases, the error caused by the assumption increases. (Rohdewald, 2016)

The wavefront method, which in Rayfract® can be considered as an optimized version of the GRM (Generalized Reciprocal Method) described by Palmer (1980) is a technique for interpreting refraction arrival times. The method creates a wavefront system from surface arrival times (Aldridge and Oldenburg, 1992). Huygens' Principle, which states that every point on a wavefront can be considered to be a secondary source of spherical waves (Reynolds, 2011), is used in reverse to reconstruct wavefronts from the surface arrival times (Aldridge and Oldenburg, 1992). The software generates a local receiver separation at each receiver station, rather than allowing a user-specified receiver separation. The receiver separation is estimated from forward and reverse wavefront emergence angles. The receiver separation can vary laterally along the profile. Due to this the method reliably images refractors with high relief (Rohdewald, 2016).

Prior to making the Plus-Minus and wavefront model the crossover points, in Rayfract® referred to as branch point, are picked to create a layered model. When converting the travel times into a start model the overburden and base filter parameters are chosen. Adjusting the overburden and base filter width affects the width of the smoothing filters for elevation and velocity of refractor 1 and 2 respectively. For difficult and undulation apparent refractor topography a higher value is recommended (Rohdewald, 2016)

As well as the integrated methods of creating start models, traditional interpretations can be used as start models when loaded into the program as grid files. When using a start model not generated by Rayfract® the software creators does not guarantee the reliability of the result (Rohdewald, 2016).

The maximum velocity update parameter limits the allowed relative velocity change in a cell from one iteration to the next. If the velocity update calculated is greater than allowed, the parameter limits the update and the velocity is set to the maximum allowed. The maximum velocity update may range from 0.01 % to 35 %, a higher maximum velocity update allows for a more varied velocity grid. (Rohdewald, 2016)

The wavepath frequency is by default set to 50Hz. The wavepath frequency is the central frequency of the Ricker wavelet that is used to adjust the wavepath misfit gradient amplitude. The wavepath frequency can be edited by the user (Rohdewald, 2016).

The wavepath width is specified in percent of one period of the wavepath frequency. The parameter can be set to a number between 0.1 and 100 %. An increase in the wavepath frequency causes a wider wavepath, which results in a smoother velocity model. To increase the resolution of a high velocity basement the wavepath width can be decreased. When decreasing the wavepath width, one should be aware that artifacts from the raypath might influence the final model. (Rohdewald, 2016)

To achieve a better resolution in the velocity model created by the tomographic inversion, the smoothing settings can be edited. Full smoothing is the default setting. When ticking of 'minimal smoothing' instead, a narrow averaging filter is applied to the updated velocity grid after each iteration. When using the 'minimal smoothing' setting the final model will show grater detail than when using 'full smoothing' but the risk of artifacts is increased. (Rohdewald, 2016)

The DeltatV and WET tomography inversion requires a shot per every sixth receiver as a minimum. To receive the best results, shots per every third receiver or closer is recommended (Rohdewald, 2016). If two sections are going to be connected, and interpreted as a continuous profile in Rayfract® there needs to be an overlap of at least one recording station between two adjacent sections (Rohdewald, 2016). Recording shots with a greater offset reduces the need to overlap the spreads to obtain a good coverage. It is recommended to use an receiver station overlap of 25 % when processing multiple sections as one profile (Rohdewald, 2016).

As the default setting the steepest descent method is chosen for the WET inversion. The steepest descent method is more robust than the conjugate gradient method when handling noisy first break picks with reciprocal travel time errors and recording

geometry errors. Choosing conjugate gradient may yield a sharper image with lower RMS error with fewer WET iterations. (Rohdewald, 2016)

There are two ways to run the WET inversion. The default setting is with the WET runs active unpicked, this is referred to as single run inversion. This setting runs all the iterations with the same parameter settings (Rohdewald, 2016). When the WET active run settings is activated the wavepath width and frequency can be changed for each WET run, referred to as multi run inversion. The first WET run is using the selected start model. The next WET run is preformed using the output tomogram of the previous WET run as its start model (Rohdewald, 2014).

3. Performed measurements

During the field work at the Fen Complex three profiles of resistivity measurements and two profiles of refraction seismic surveys where executed. Due to the survey not being performed with the required overlap in receiver stations, Profile 1 of the seismic survey is divided into seven sections. The Regional Head Geologist, Sven Dahlgren, has also provided information from boreholes from the area that will be presented and used to aid the interpretations.

3.1 Resistivity measurements

The resistivity data at the Fen Complex was acquired using an ABEM Terrameter LS programmed to perform multi-gradient array measurements. Three resistivity profiles with 5-meter electrode spacing were gathered at the Fen Complex. The resistivity data was inverted using RES2DINVx64. The data was inverted using both the 'L_1' and the 'L_2 norm'. When using the RES2DINVx64 software the color scale can be changed to emphasize the variation in the apparent resistivity.

All three profiles contained some measurements that yielded negative resistivity. The negative values were removed prior to inverting the data. An overview of the total measured points and points used in the inversion are displayed in Table 4. 34 points were removed from profile 1, three points from profile 2 and 33 points from profile 3. The low number of removed points indicates good data quality.

Table 4: Total of measured points in the resistivity survey and points used in inversion for profiles 1-3 at the Fen complex. The removed point had negative values that would affect the inversion results.

	Profile 1	Profile 2	Profile 3
Total measured points	7072	1168	2644
Points used in inversion	7038	1165	2611

During the data gathering GPS coordinates at each measuring station were collected, which resulted in a spacing of 100 m along the profile. Based on the GPS coordinates and the maps of the area, the location of each electrode was calculated. Using LiDAR data collected by Blom Geomatics AS in 2010 (Blom, 2011), the topography of each electrode position was extracted using the ArcGIS software. The topography at each electrode was added into the Res2Dinvx64 software making the inversion incorporate the difference in topography in the calculations.

3.2 Refraction seismic

In the project prior to this Master's thesis the refraction seismic data was interpreted using Hagedoorn's method and a model was created. Jan Fredrik Tønnesen at NGU also created an interpretation, which will be used as the traditional interpretation in this thesis.

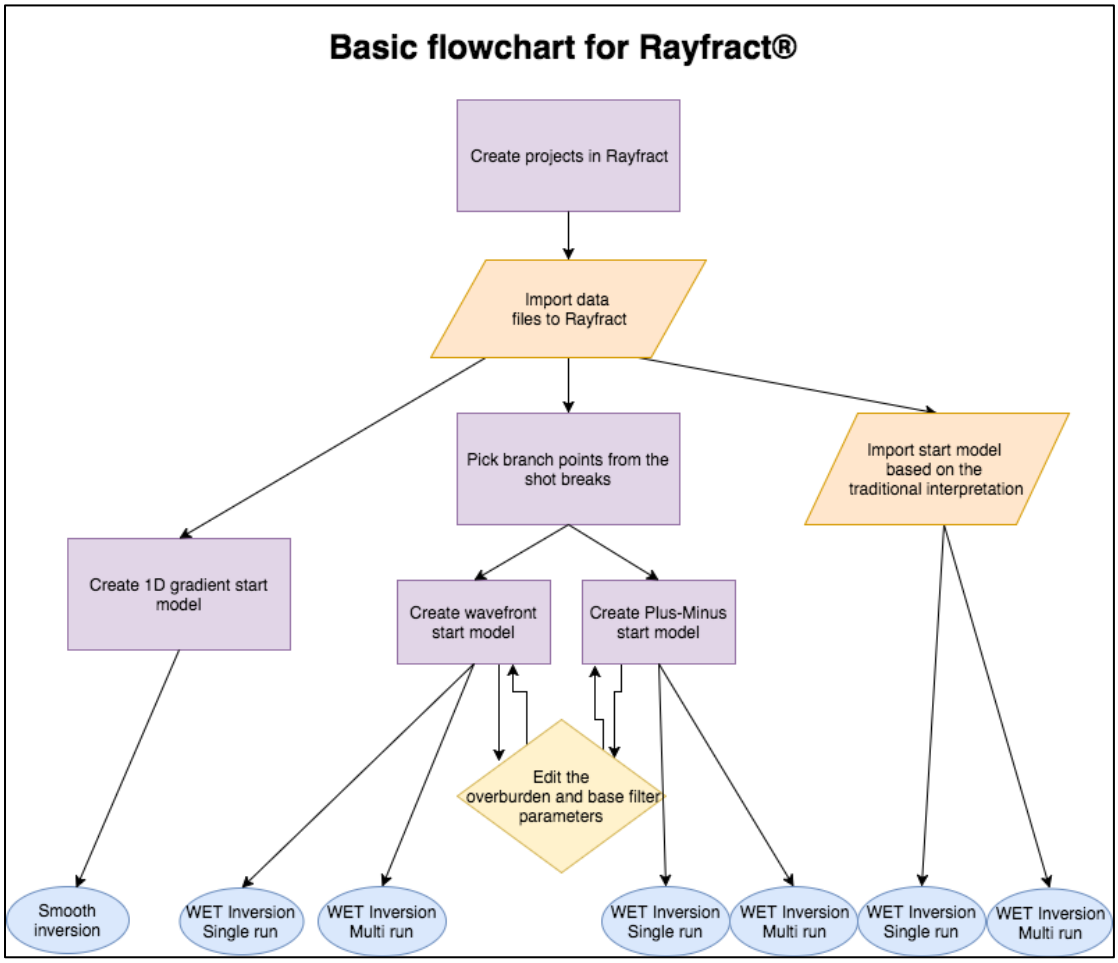

Figure 7: Flowchart of the operations performed in Rayfract®.

3.2.1 Preparing seismic data for Rayfract ®

In order to import data into the Rayfract® software, which is the first step after creating the projects in accordance to Figure 7, the input data must be in the .ASC, .SHO and .COR format. The .ASC files must contain 4 columns, in which the headers are shot number, shot station, receiver station and first breaks. The shot numbers are represented by integers that indicate the position of the shot. Shot station is the shot position in meters divided by the geophone spacing. In example if the shot position is 30 meters from the start of the section, and the geophone spacing is 5 meters, the shot station would be 30 m/5=6 m. The receiver station is the geophone number along the

section starting with zero. The last column, the first breaks must be in seconds. The seismograph delivers its results in milliseconds and a conversion is mandatory.

The .SHO file has 12 columns with headers; shot number, shot X, shot Y, shot Z, hole depth, uphole time, correction, shot delay, trigger delay, shot station, shot inline and lateral offset. The columns for hole depth, uphole time, correction, shot delay, trigger delay, shot inline and lateral offset were set to zero. Shot number and shot station is the same as in the .ASC file, while the Shot X, Y and Z columns are filled with the WGS 84 - UTM 32 N coordinates and elevation of the shot positions. The coordinates where captured using a hand held GPS for all the shot stations during the data collection while the elevations have been extracted through a LiDAR raster in GIS. Bjørn Eskil Larsen at NGU performed the extraction of the elevation from the LiDAR raster.

The .COR file has 4 columns with headings station number, X coordinates, Y coordinate, and elevation. The station number refers to the geophone number, starting with zero. The X- and Y coordinates and elevation are the WGS 84 - UTM 32 N coordinates and the elevation of the geophones. The exact location of the geophone was not captured, to calculate the coordinates Bjørn Eskil Larsen constructed a line from the first to the last shot position and created points with a 2.5 meter separation along the line. Every other point was deleted to simulate the location of each geophone. This is not as exact as it would have been to have the exact location of each geophone captured by the GPS, but for this purpose it was considered good enough.

3.2.2 Start models

The start models created for each section of the seismic survey are shown in Table 5. As stated previously the wavefront start model was not eligible for all sections due to the scarce shot placement. As a result, three start models were created for profile 1/

sections one, four and five, and four start models for profile 1/ sections two, three, six and seven and profile 2.

Table 5: The start models created for each section of the seismic survey.

Section	Traditional interpretation	Plus-Minus start model from Rayfract®	Wavefront start model from Rayfract®	1D-Gradinet start model from Rayfract®
Profile 1 Section 1	Yes	Yes	No	Yes
Profile 1 Section 2	Yes	Yes	Yes	Yes
Profile 1 Section 3	Yes	Yes	Yes	Yes
Profile 1 Section 4	Yes	Yes	No	Yes
Profile 1 Section 5	Yes	Yes	No	Yes
Profile 1 Section 6	Yes	Yes	Yes	Yes
Profile 1 Section 7	Yes	Yes	Yes	Yes
Profile 2	Yes	Yes	Yes	Yes

1D-Gradient

As recommended by the Rayfract® user manual the first process conducted was the creation of a 1D-Gradient start model. The 1D-Gradient start model was used to run a smooth inversion. The 1D-Gradient start model and inversion was conducted using the default parameters of the software. The flowchart in Figure 7 illustrate that this is the simples inversion Rayfract® cam perform.

Rayfract® generated Plus-Minus model

After the seismic data was imported info Rayfract®, branch points where picked. The branch points were picked for the first interface, creating a two-layer model.

According to the traditional interpretation the area has three distinctive layers, but due to the scarce placement of shots, Rayfract® would only allow for two layer models. After picking the branch points the overburden filter and base filter values were adjusted to create different start models where vertical and horizontal structures are enhanced.

The overburden and base filter for the Plus-Minus and wavefront start models were set to the values presented in Table 6, creating 5 different start models. The start models and their inversions will be presented in the results.

Table 6: Overburden and base filter values for the Plus-Minus and wavefront start model

Overburden filter	Base filter
2	2
2	10
5	5
10	2
10	10

Wavefront model

As shown in Figure 7 the branch point picking is also a prerequisite in order to create the wavefront start models. The wavefront modeling is more sensitive to the shot to receiver ratio than the Plus-minus method; therefore it was not possible to model all the sections using the wavefront method. After picking the branch points between the first and second interface, the software generates the start models. The same parameters for overburden and base filter were tested for the wavefront model as for the Plus-Minus model. The values are presented in Table 6.

Traditional interpreted start model

To be able to use the interpretations created by Jan Fredrik Tønnesen as start models in Rayfract® the interpretation has to be in a .GRD format. The .GRD format is a grid format where each cell in the grid has a value; the value in each grid point represents

the velocity in that point. To create the .GRD files from Tønnesen's interpretation the Surfer 12 software was used.

The models were constructed by creating grids with the interpreted velocity using the 'function' function and merging them together using the 'mosaic' function in Surfer. Each layer was shaped using .BLN files created for the layers. Using the 'blanking' function values above the limit of the .BLN file were removed. This process was repeated for all seven sections of Profile 1 and for Profile 2. In order to be compatible with the Rayfract® software all sections has to be from 0-120 m, not their original location.

After the traditional interpretation was transformed into grid files they were imported into Rayfract® as is described in the flowchart in Figure 7. After importing the data and choosing the grid as the start model, the WET inversions were run.

Inversions

The Plus-Minus, wavefront and traditional start model was inverted using the WET inversion with the single and multi run.

For Profile 2 and Profile 1 Section 4 the inversions were run multiple times changing the parameters for smoothing, wavepath frequency and wavepath width and with the steepest descent and conjugate gradient inversion techniques. This was done to investigate how changing the parameters affect the produced velocity model. Profile 2 and Profile 1 Section 4 were chosen to investigate further due to the fact that they present interesting features in the traditional interpretation and have decent shot coverage.

The wavepath width for the multi run WET was tested descending between 30-1 %, 30-5 %, 30-10 % and 30-15 % with a wavepath frequency of 50 Hz. Each run has its

assigned wavepath width. A detailed overview is provided in Table 7. For the WET single run inversions the wavepath widths of 3, 10 and 15 % were used.

Table 7: Presentation of wavepath widths for each run with the multi run setting for each interval.

Wavepath width range	Wavepath widths for each run
30-1 %	30, 22, 16, 10, 7, 5, 4, 3, 2, 1
30-5 %	30, 25, 20, 15,10, 9, 8, 7, 6, 5
30-10 %	30, 24, 19, 16, 15, 14, 13, 12, 11, 10
30-10 %	30, 28, 26, 24, 22, 20, 18, 17, 16, 15

To test the effect of the wavepath frequency, frequencies of 25, 50, 100 and 200 Hz were tested in inversions. In these inversions the wavepath width was set to 30-1 % for the multi run WET inversions.

To be able to compare the results, one parameter was changed while the others were kept constant. The resulting models, their ray coverage and the RMS error was compared to find the most likely model of the subsurface. The result of the effects of the parameters will be presented in the results and discussed.

The remaining profiles were inverted using the technique with the best results for Profile 1 Section 4 and Profile 2.

3.3 Boreholes

Table 8: Location and depth to bedrock of boreholes at the Fen Complex in WGS 84 - UTM 32 coordinates.

Name	Easting	Northing	Depth to bedrock
Fen SKOLE1 2016	517260.17046	570350.5320	7
Fen FEN2 2016	517167.1127	657034.4524	16.2
Fen TEIG2 2016	516995.7567	6570439.6922	6.25
Fen HLA6 2016	515692.9956	6569793.6241	15.1
Fen HLA 4 2016	515512.7339	6569420.9330	10.8
Fen MTGN5B 2016	51535.4963	6569295.2393	5.8
TUFTE-1	516381.164	6570376.327	4.3
TUFTE-3	516585.211	6570107.933	>18 (not reached)
TUFTE-4	516451.438	6570312.827	8.2
TUFTE-5	516676.652	6570331.454	8.4
TUFTE-6	516680.885	6570501.634	7.9
TUFTE-7	516633.471	6570230.700	>13.5 (not reached)
TUFTE-9	516355.764	6570333.94	1

Multiple boreholes have been drilled at the Fen Complex to investigate the depth to the bedrock and to map the unique geology of the area. Geir Viken from NGU has performed the drilling in cooperation with Regional Head Geologist, Sven Dahlgren. The boreholes in close proximity to the seismic surveys and resistivity measurements are presented in Table 8. While drilling, the soil covering the bedrock was characterized as it ascended form the borehole. The soil was characterized as very wet mud and hard silt. The geological interpretation of the soil in the area claims that the soil is mostly marine sediments (Dahlgren, 2016). The data is from the report 'Fensfeltet – Kjerneboringer Tufte 2016' by Sven Dahlgren and received through personal communication with Dahlgren. The data from the boreholes will be used to substantiate the results of the seismic survey and resistivity measurements.

4. Results

In this section the results of the resistivity measurements and seismic survey will be presented. Figure 8 is a map showing the location of the seismic surveys, resistivity measurements and boreholes. The map is created using the Surfer 12 software with base maps from Kartverket (2007). The topographic contour lines have a 5-meter interval. The seismic profiles are marked with red lines on the map. Seismic profile 1 is the longer of the two seismic profiles. The resistivity profiles are marked with green on the map. Resistivity profile 1 is the longest of the resistivity profiles, resistivity profile 2 is the short profile in the east and resistivity profile 3 is the resistivity profile furthest north. The boreholes are marked as blue stars.

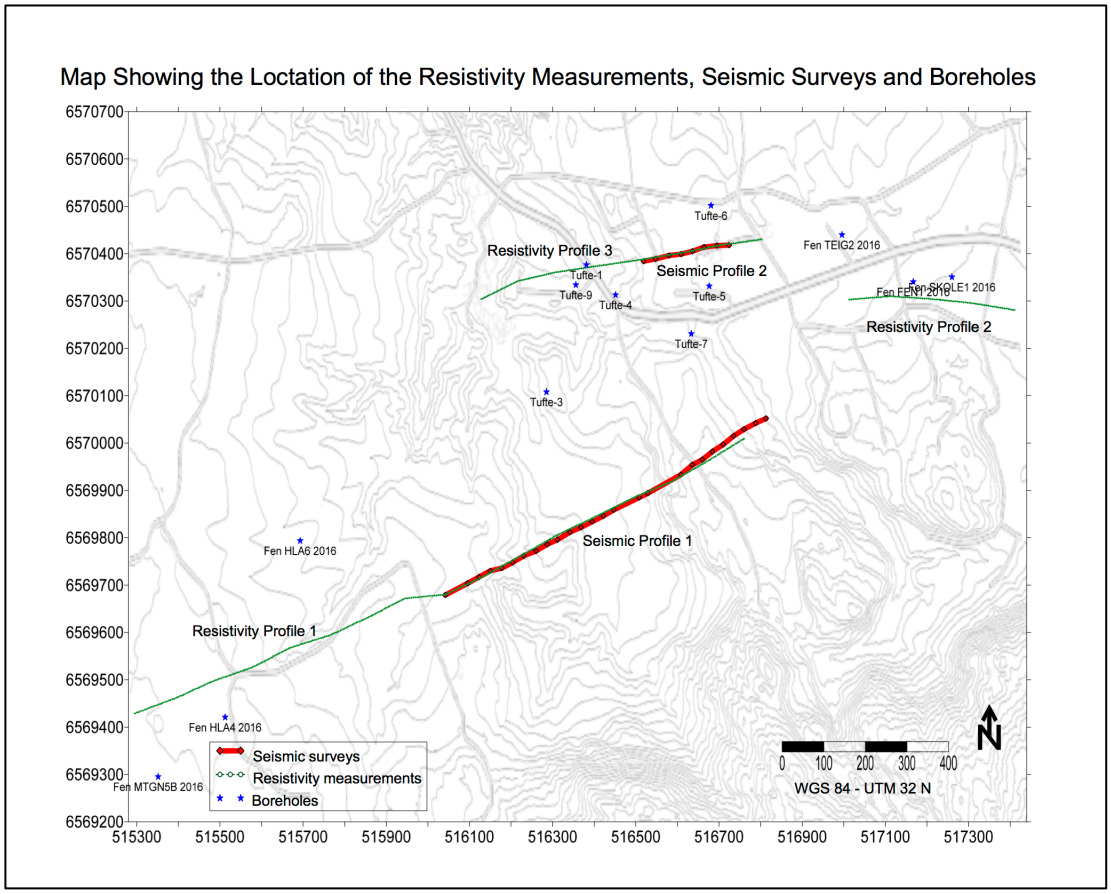

Figure 8: Map showing the locations of the resistivity measurements, seismic surveys and boreholes. The green points are the resistivity measurement points, the red lines the seismic profiles and the blue stars represents the boreholes. The map is created using Surfer 12 software.

4.1 Resistivity measurements

This section will present the processed resistivity measurements from the Fen Complex.

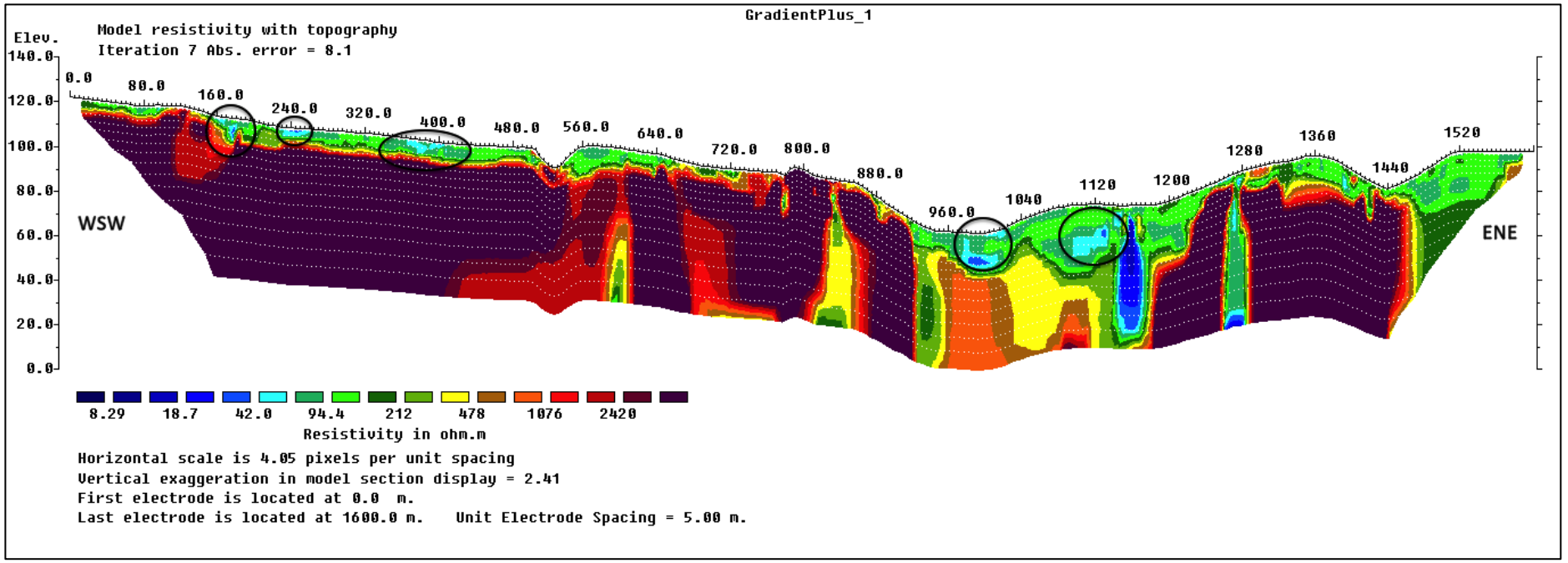

Figure 9: Resistivity profile 1 inverted with smoothing settings, 'L_2 Norm'. Color scale to detect varieties in soil.

Figure 9 displays profile 1 inverted with the 'L_2 norm' with a color scale set to detect varieties in soil. Based on the resistivity classifications as defined by Solberg et al. (2008) in Table 2 the areas with black circles at 160, 240, 400, 1000 and 1120 m could be considered as possible areas of quick clay. The resistivity surrounding the area is not in the resistivity range of 1-10 Ωm, which it should be if it was unleached marine clay. This challenges the interpretation that quick clay is present, due to the way quick clay is formed. The resistivity of the soil is in the in the range of 100 Ωm, this can according to Solberg et al. (2010) be, in addition to quick clay, dry crust clay or saturated sand and gravel. If the areas are quick clay, they are relatively small but at places with some degree of dip in the topography. This may cause instabilities if there are invasive changes to the usage of the area. At the time of data acquisition the area is used for farming, grazing areas and scarce housing which does not require massive displacement of the soil. If invasive changes to the usage of the land are considered, further geotechnical investigation should be performed to ensure the stability of the soil. The absolute error of this inversion to the pseudosection is 8.1 %. The degree of error suggests that the fit of the model is good according to the classification by Rønning et al, 2017.

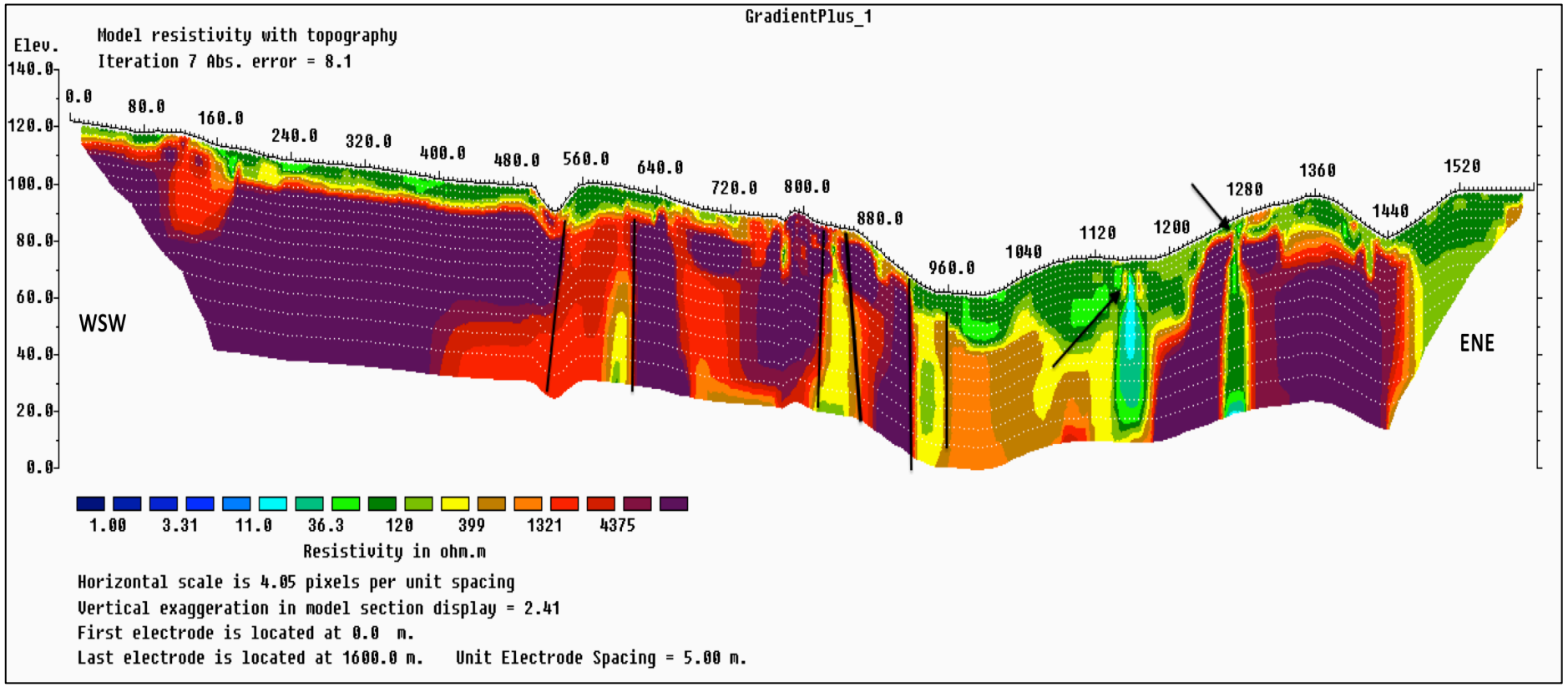

Figure 10: Resistivity profile 1 with a smoothing inversion, 'L_2 norm'. Color scale set to detect quality of bedrock.

In Figure 10 the color scale of profile 1 is set to determine quality of bedrock. It is plausible to assume that the dark purple and maroon areas are, based on the classification in Table 1, areas of good quality bedrock while the areas in between the black lines can be investigated further as fractured bedrock or low quality bedrock, due to the resistivity values. The low resistivity of the bedrock at 560 m, around 2000 to 3000 Ωm, makes the section an interesting area or investigation for a possible fracture zone based on the characterization of weakness zones and rock quality presented in Table 1. The area around 560 m could possibly be a fault zone where the bedrock is fractured and weathered. The area marked with black lines right before the 880 m mark is also interesting and shows exceptionally low resistivity, the yellow color yielding less than 400 Ωm. According to Table 1, the resistivity values can correspond to an instable rock mass with water leakage. The black arrow at and 1280 m indicates a very low resistivity area. This coincides directly with a road crossing the profile; the extent to which this will affect the resistivity is unknown, but it is implausible that it is the sole reason for the low resistivity. Therefor it can either be an anomaly in the resistivity due to infrastructure, wires, pipes etc. that is running along the road, an indication of another fracture zone, moraine sediments, or a combination. The arrow at 1150 m indicates an area with low resistivity. The low resistivity area may be interpreted the same way as the area around 1280 m, as either buried infrastructure or as a fault.

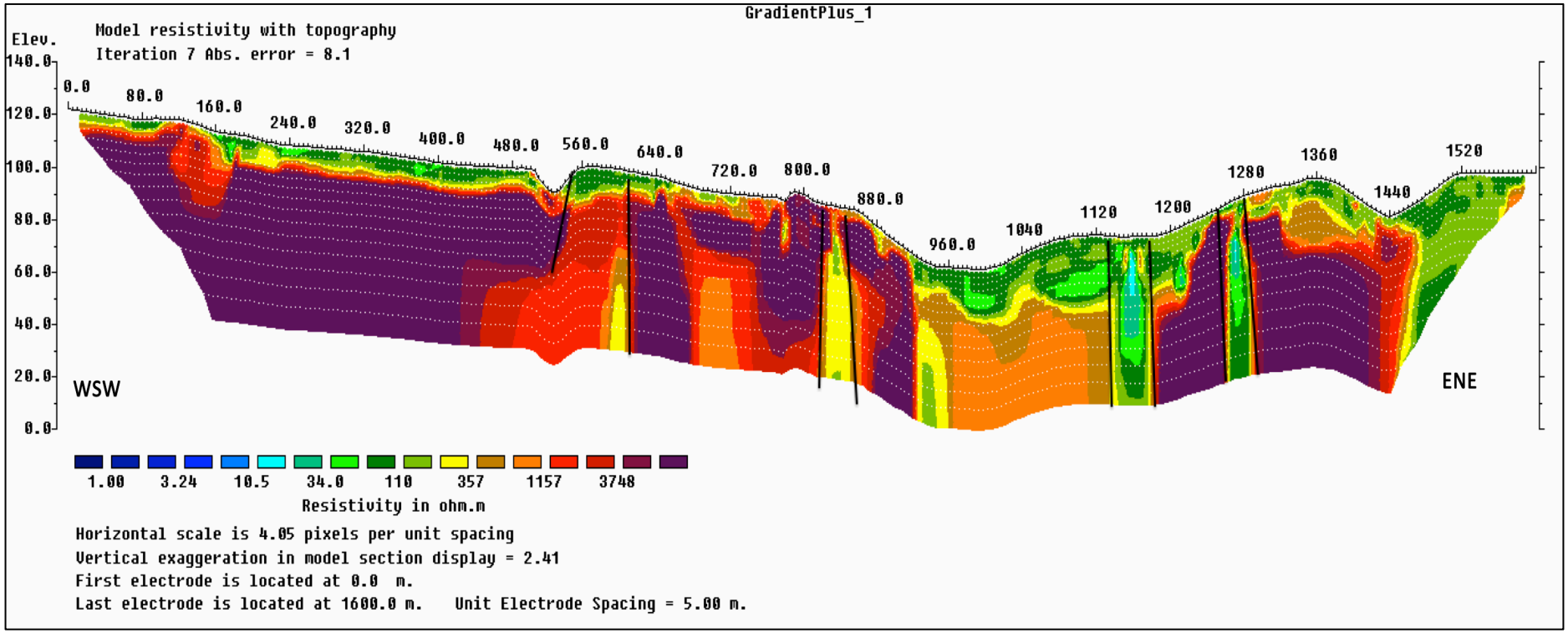

Figure 11: Robust inversion, 'L_1 norm', of profile 1. Color scale set to detect major differences in resistivity.

Profile 1 is in Figure 11 inverted based on the robust inversion, 'L_1 norm'. The inversion shows the same areas with low resistivity as the smooth inversion, 'L_2 norm', in Figure 10 yet with sharper boundaries, as the theory behind the inversion suggest. This is especially visible at the area between 960 and 1120 m where the boarders between the resistivity values are sharper. From the robust inversion it is possible to detect what could be the interface between soil and bedrock. In the area from 160 to 640 m the interface seems to be at around 10 m, with local variations. From 1160 m towards the 1280 m mark the depth to the soil bedrock decreases to where it can be interpreted to approximately 15 m. The area between 960 and 1120 m with resistivity in the range of 399 to 1321 Ωm is an interesting area. The resistivity indicates that the bedrock should be very fractured with water leakage, but an interpretation can also be that this is a moraine.

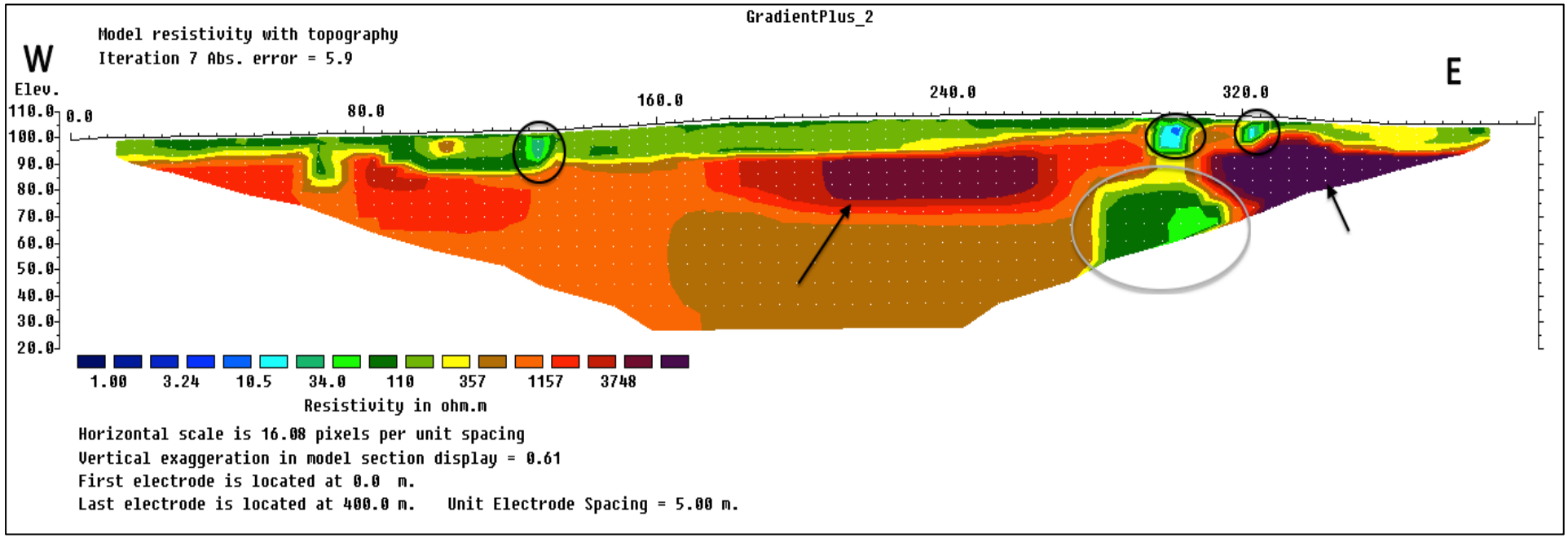

Figure 12: Profile 2 inverted with the robust model 'L_1 norm

The second profile inverted based on the robust model is presented in Figure 12. The black circles indicate where the possible quick clay or leached marine clay is located. As for profile 1, the absence of resistivity in the range of 1-10 Ωm, representing unleached marine clay, creates doubt to the presence of quick clay. The lack of unleached marine clay can support the interpretation that the soil is cry crust clay or saturated water and gravel. The two black circles close to 300 m coincide with a road, as discussed with profile 1 it is plausible to link the low resistivity values to infrastructure related to the crossing road. This infrastructure may also be the reason for the deeper anomaly located under the black circle at 300 m indicated with a grey circle. Based on the higher resistivity on both sides of the anomaly there is no indication that an area with values as low as 34 Ωm should be recorded there.

The varying resistivity values of the bedrock in the area, can suggest that either there is a bedrock boundary present, or that the bedrock to the west of the anomaly at 300 m is heavily fractured. The resistivity is higher in the bedrock towards the east than towards west of the profile. The lens of high resistivity, which the black arrow points to, located around 240 m may suggest that the anomaly at 300 m affects the section than to a greater extent than predicted. Another interpretation could be that the area circled in grey is not an effect of the infrastructure but may indeed be an area of coarse soil.

The depth to the soil bedrock interface in profile 2 can be interpreted to be approximately 15 m under the 160 m mark decreasing toward the east. The absolute error in this model from the pseudosection is 5.9 %, which makes the inversion of profile 2 a better fit its pseudosection than profile 1 is to its pseudosection.

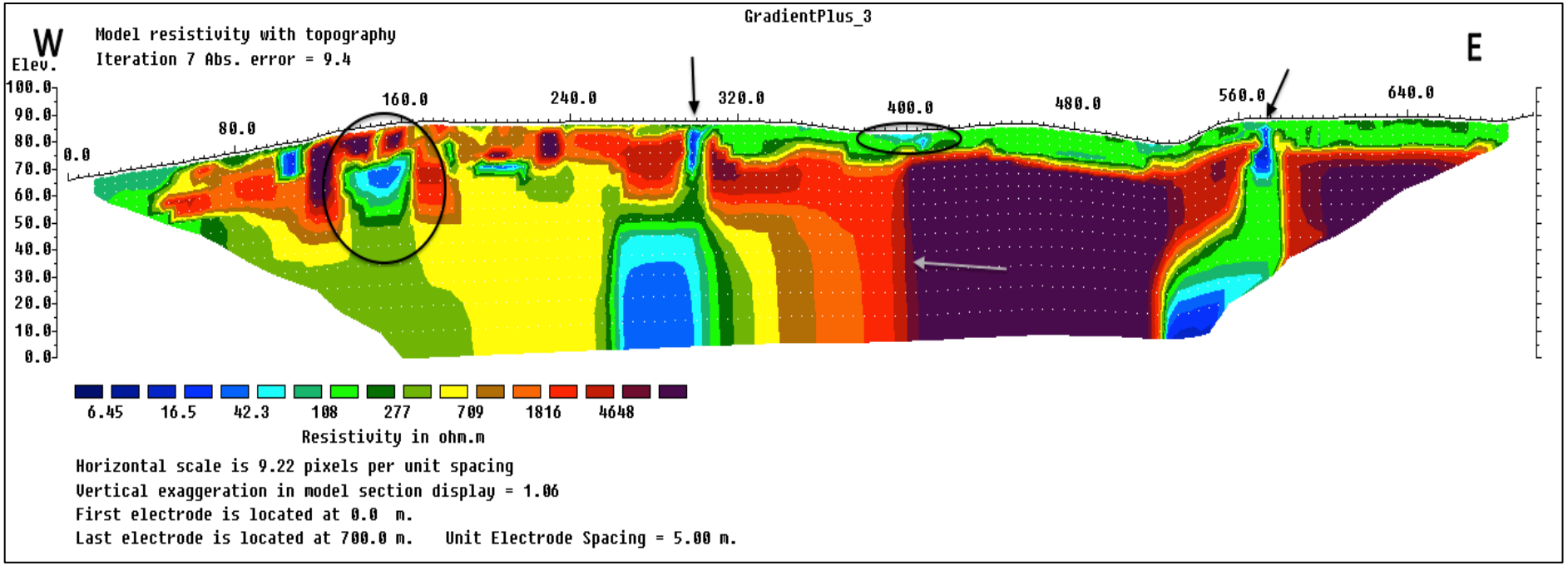

Figure 13: Profile 3 inverted using the robust model 'L_1 norm'.

Profile 3 is a profile that starts in an inhabited area and the profile crosses a road after approximately 100 m. The infrastructure seems to have influenced the profile in multiple areas. Figure 13 shows the robust, 'L_1 norm', inversion of profile 3. The black arrows at 300 and 575 m show low resistivity values that could be an effect of the infrastructure along crossing roads. Both anomalies seem to affect the profile to great depths. The anomaly marked by the black circle at 160 m, suggest a low resistivity zone beneath areas with higher resistivity. A pipeline buried at approximately 15 m depth, which 'steals' the applied current, may cause this anomaly. The black circle around 400 m might be an area of quick clay due to its resistivity of approximately 60 Ωm, when consulting the classification of Table 2. The soil in the area could be defined as dry crust clay or water saturated sand and gravel, due to the resistivity values of 100 Ωm (Solberg et al., 2010). The lack of resistivity values of 1-10 Ωm, unleached marine clay, challenges the interpretation of quick clay. If the interpretation of quick clay in the top layer of this flat area would be correct, it would probably not be considered a hazard, unless it stretches far in the north-south direction, which is impossible to tell from the resistivity profile. The grey arrow, beneath the 400 m mark, points to a sudden change in resistivity from good solid bedrock to possible fractured bedrock of lower quality. The deep anomaly at 300 m may influence the sharp boundary causing the bedrock to appear with lower apparent resistivity values than the true resistivity, but it may also be a boarder between two different bedrocks.

4.2 Refraction seismic

This section will present the different start models and inversions created in Rayfract® and the traditional interpretation of the profiles.

4.2.1 1D-Gradient inversion

As stated previously the generated 1D-Gradient start model is simplest start model in Rayfract®, the start model generated from the data from Profile 1 Section 4 is presented in Figure 14. The start model has velocity increasing with depth evenly throughout the model. The velocity increases from 400 m/s at the top to 5000 m/s at the bottom.

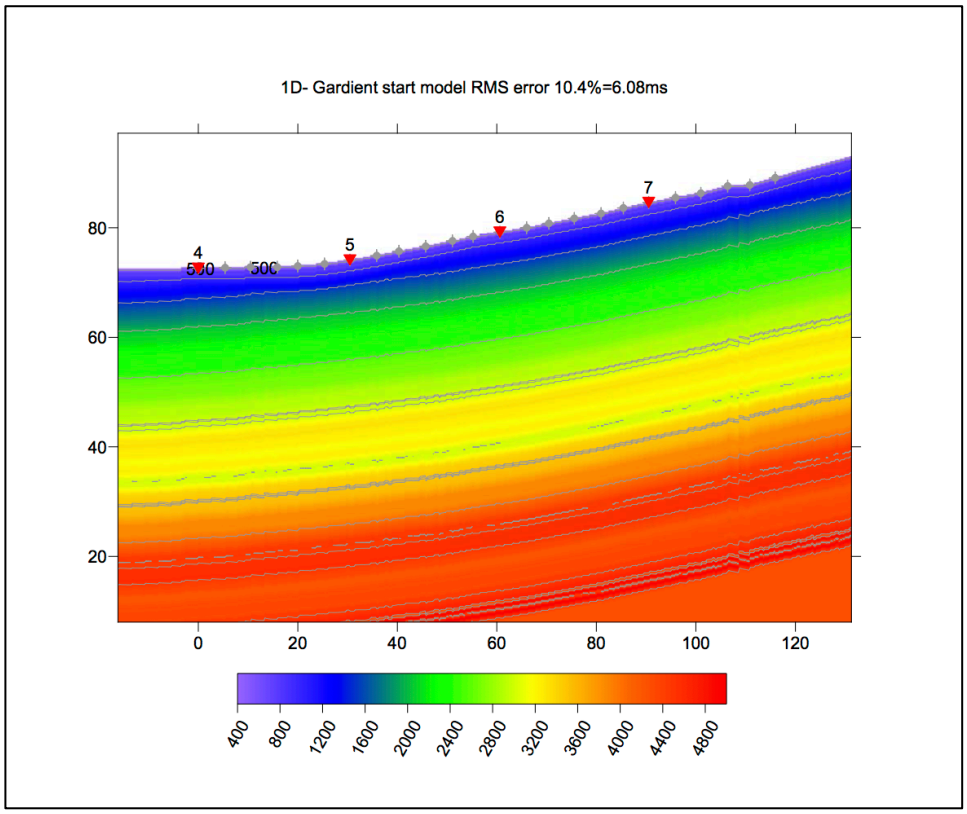

Figure 14: 1D-Gradient start model for Profile 1 Section 4.

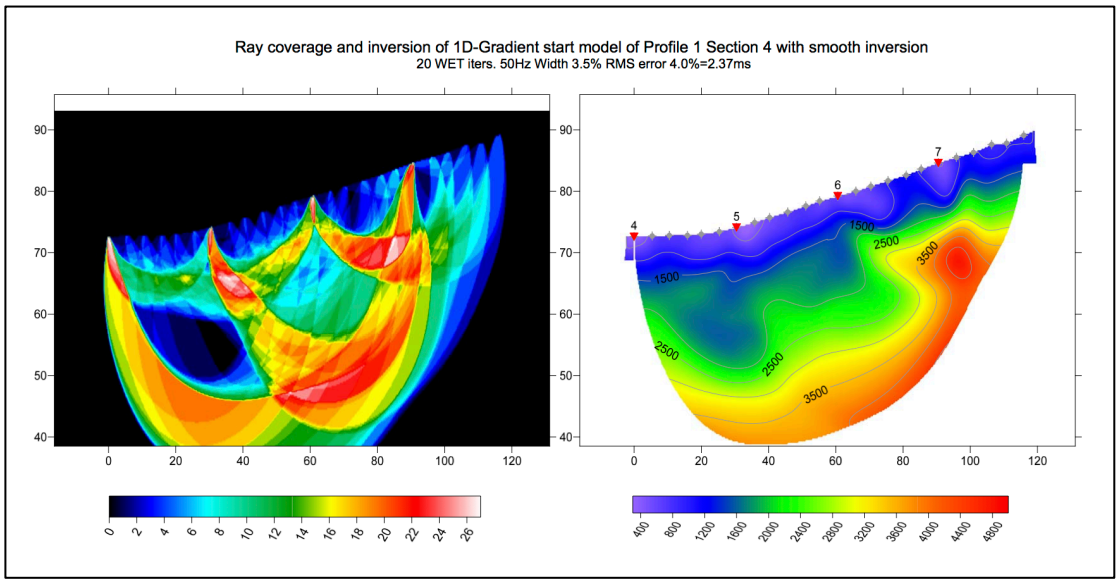

Figure 15: Profile 1 Section 4 smooth inversion based on the 1D-Gradient start model. The coverage diagram is to the left and the inverted model to the right.

The smooth inversion of the 1D-Gradient start model and the ray coverage diagram is displayed in Figure 15. The inverted model has velocities from 300 to 5000 m/s. The velocity is higher to the right half of the model, from the 80 m mark and towards the right. The ray coverage diagram reveals that the area to the right has a higher coverage than the areas in the left part between 50 and 60 m vertically and 10 and 50

meters horizontally. In this area the ray coverage is as low as 1. There were 20 WET iterations in the inversion, 50 Hz wavepath frequency and 3.5 % wavepath width. The RMS error of the inversion is 4 %.

4.2.2 Generated Plus-Minus Inversion

The Plus-Minus start models generated by Rayfract® with different overburden and base filter values for Profile 1 Section 4 are displayed in Figure 16. When changing the overburden and base filter values the vertical and horizontal structures are weighted differently, which is visible in the difference in the start models. Figure 16 A) and Figure 16 G) are quite similar, the start models have lower velocity than the others, and the velocity gradually increases towards the right of the section from the 40 m mark. Figure 16 C) and Figure 16 I) are similar, with slightly higher velocity gradually increasing toward the right of the section. Figure 16 E) with overburden and base filter values equal to five differ significantly from the others with a clear change in velocity and velocity as high as 4500 m/s in the right part of the section. The inversions based on the different start model share the same features, with lower velocity in the left part of the section and higher after the 80 m mark horizontally and towards the right. In the bottom right the velocity is 5400 m/s. The depths the inversions reaches are similar, but the inversion in Figure 16 F) reaches down to 30 m vertically, about 10 m deeper than the other profiles. The low velocity zone in the middle to left part of the models indicates a weakness zone. The small increase of velocity in the left leads to the interpretation that the weakness zone ends close to the end of the profile.

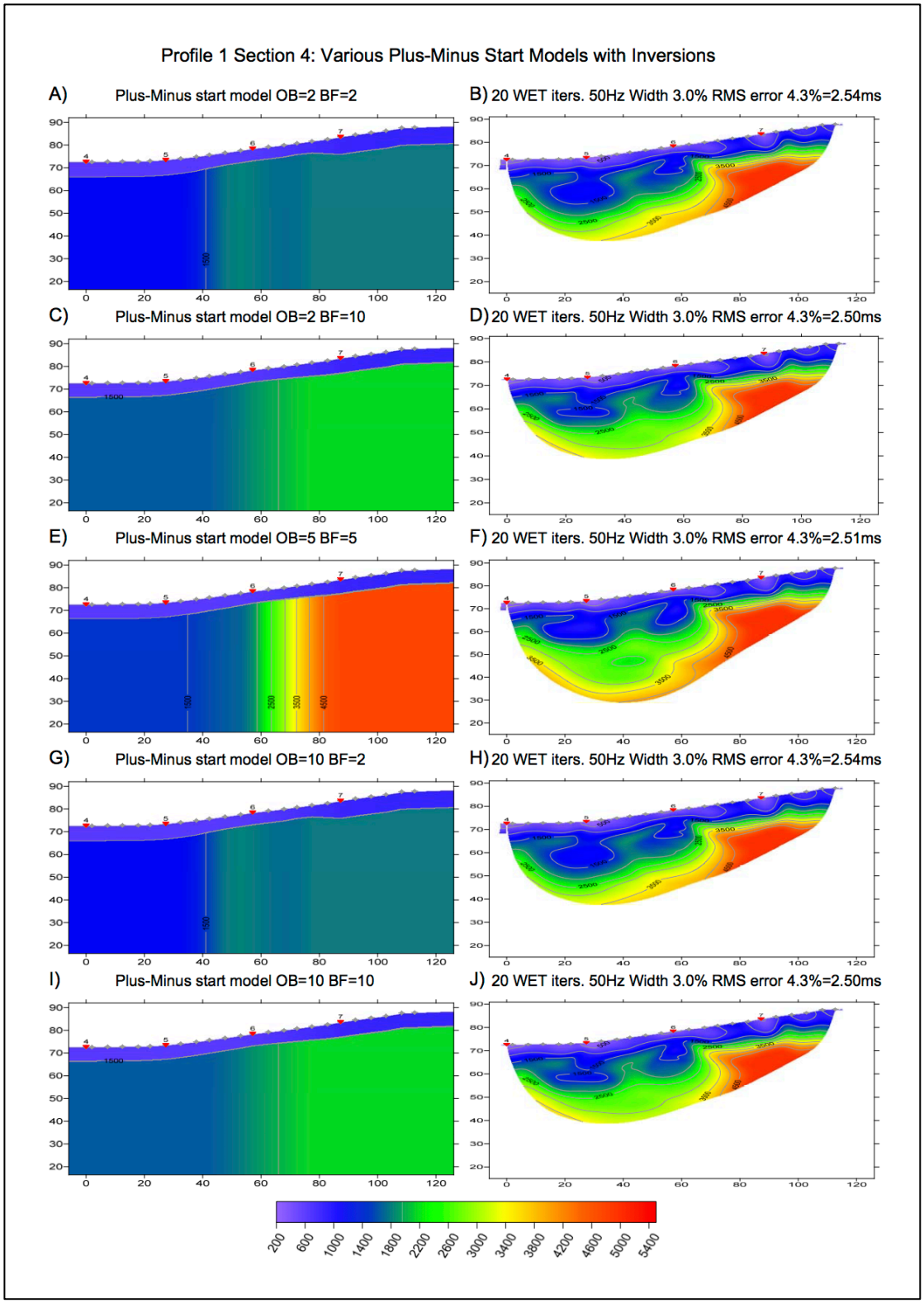

Figure 16: Plus-Minus start models and the multi run inversion with 50 Hz wavepath frequency, wavepath width from 30-1 % and 20 WET iterations. A) Plus-Minus start model with overburden filter 2 and base filter 2. B) The inversion of the start model in A). C) Plus-Minus start model with overburden filter 2 and base filter 10. D) Inversion of start model C). E) Plus-Minus start model with overburden filter 5 and base filter 5. F) Inversion of start model E). G) Plus-Minus start model with overburden filter 10 and base filter 2. H) Inversion of start model G). I) Plus-Minus start model with overburden filter 10 and base filter 10. J) Inversion of start model I).

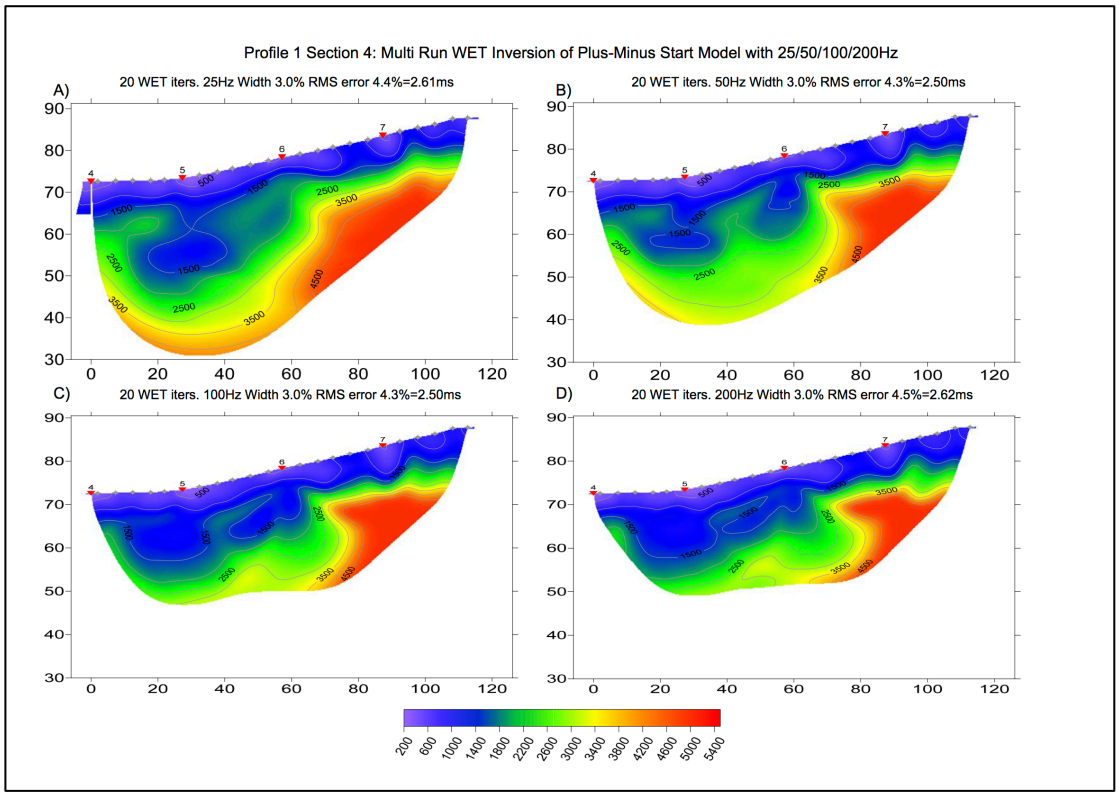

Figure 17: Plus-Minus start model of Profile 1 Section 4 inverted using the WET multi run with wavepath frequency of A) 25 Hz, B) 50 Hz, C) 100 Hz and D) 200 Hz and wavepath width from 30-1 %.

Figure 17 shows Profile 1 Section 4 inverted with different wavepath frequency settings, the velocity in all the inversions ranges from 200 to 5500 m/s. In Figure 17 A) the frequency is set to 25 Hz, this yields the deepest investigation of the subsurface. The inversion has a RMS error of 4.4 % or 2.61 ms which is somewhat higher than the RMS error in Figure 17 B) and Figure 17C) and almost the same as Figure 17 D). The inversion with 50 Hz, Figure 17 B), reaches a greater depth than the inversion with 100 and 200 Hz, Figure 17 C) and Figure 17D). Both of the inversions in Figure 17 B) and Figure 17 C) have the same RMS error of 4.3 % or 2.50 ms. The highest RMS error is in the inversion with 200 Hz wavepath width, Figure 17 D). The general appearance of the inversions is similar.

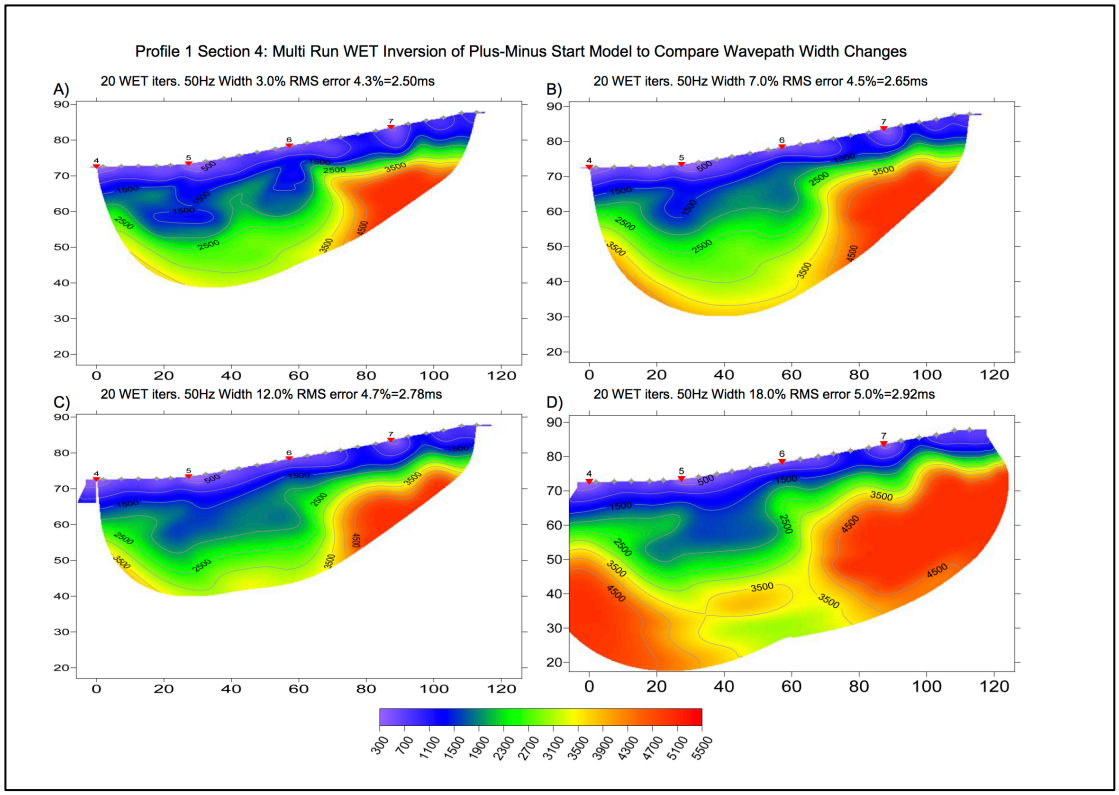

Figure 18: Plus-Minus start model of Profile 1 Section 4 inverted using the multi run inversion with different wavepath widths. 20 WET inversions and 50 Hz wavepath frequency. A) 30-1 % wavepath width. B) 30-5 % wavepath width. C) 30-10 % wavepath width. D) 30-15 % wavepath width.

When different wavepath widths are applied in the WET multi run inversion the result changes. The results of the inversions of Profile 1 Section 4 with different wavepath widths are displayed in Figure 18. The velocity ranges from 300 to 5500 m/s. In Figure 18 A) the inversion reaches the depth of 40 meters, and is at its deepest between 20 and 40 meters horizontally. The RMS error, of 4.3 % or 2.60 ms, is smaller in this inversion than in the inversions with other wavepath widths. In Figure 18 B) the depth of investigation is greater than in Figure 18 A), and the velocity in the lower middle section is higher. The general form of the two inversions is similar. Figure 18 C) has the wavepath width set to 30-10 %. Figure 18 D) is the inversion that reaches the greatest depth, 20 meters; it also holds the greatest RMS error. The error is 5 % or 2.92 ms. In this inversion there are zones of high velocity both in the left and in the right of the profile with a zone of lower velocity dipping towards the left from 20 to 80 m horizontally. Within the low velocity zone there is a high velocity zone encapsulated, this is an unlikely geological event.

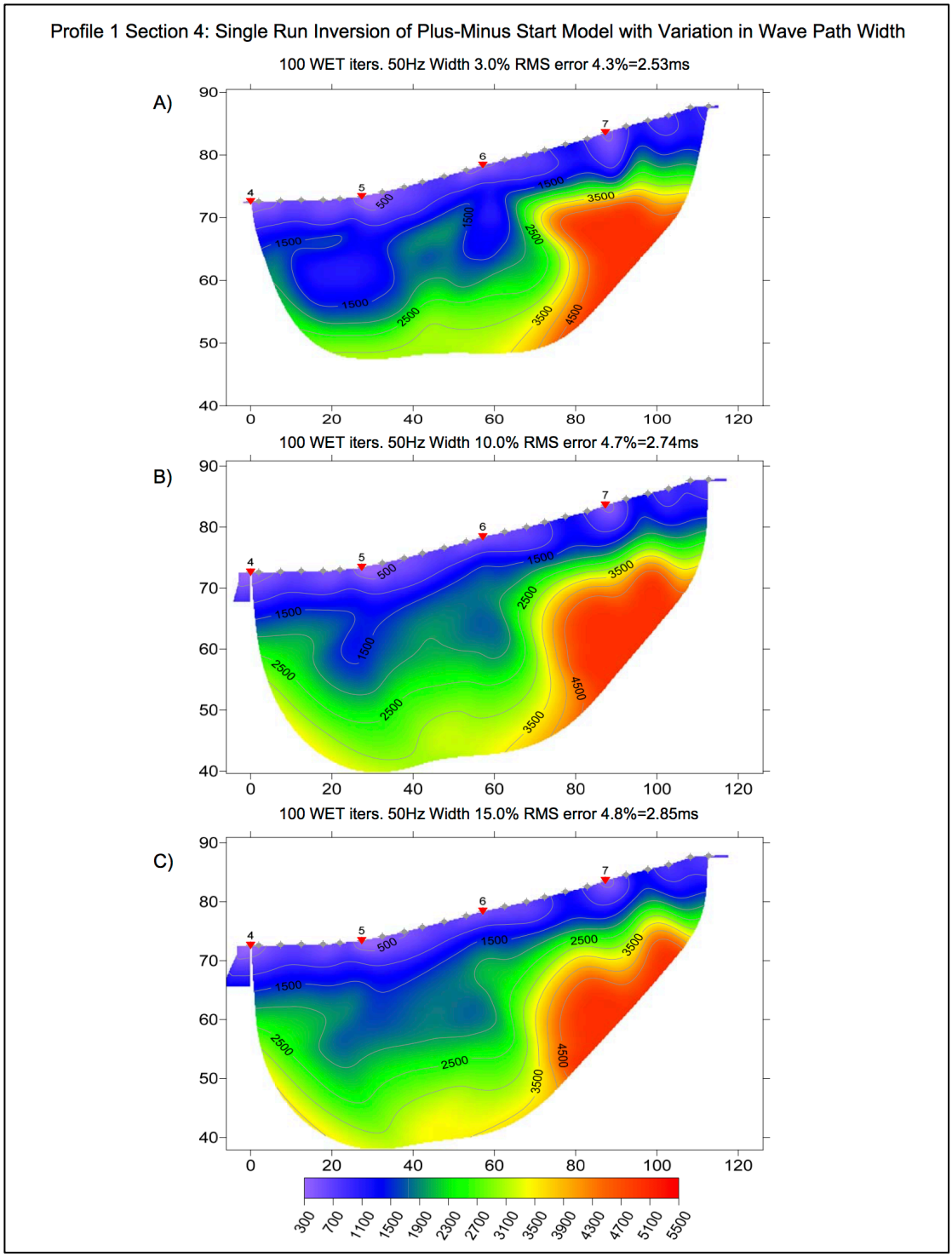

Figure 19: Inversions of Profile 1 Section 4 using the Plus-Minus start model with WET single run, 100 WET iterations and 50 Hz wavepath frequency. A) 3 % wavepath width. B) 10 % Wavepath width. C) 15 % Wavepath width.

The single run inversions with 50 Hz wavepath frequency are presented in Figure 19. 100 WET iterations were performed. The velocity in the inversions ranges from 300 to 5500 m/s. The inversions were run with wavepath widths of 3, 10 and 15 %. The inversion with 3 % wavepath width is Figure 19 A). At its deepest this inversion

reaches 50 m, which is shallower than the inversion using 10 and 15 % wavepath width. Figure 19 B) is the inversion with 10 % wavepath width and Figure 19 C) is inversion with 15 % wavepath width. Both inversions reach the depth of 40 m, and the high and low velocity zones correspond with the ones in Figure 19 A). It is worth noticing that the RMS error increases with slightly increasing wavepath width, from 4.3 % in the inversion with 3 % width to 4.8 % in the inversion with 15 % width.

4.2.3 Inversions based on the traditional start model

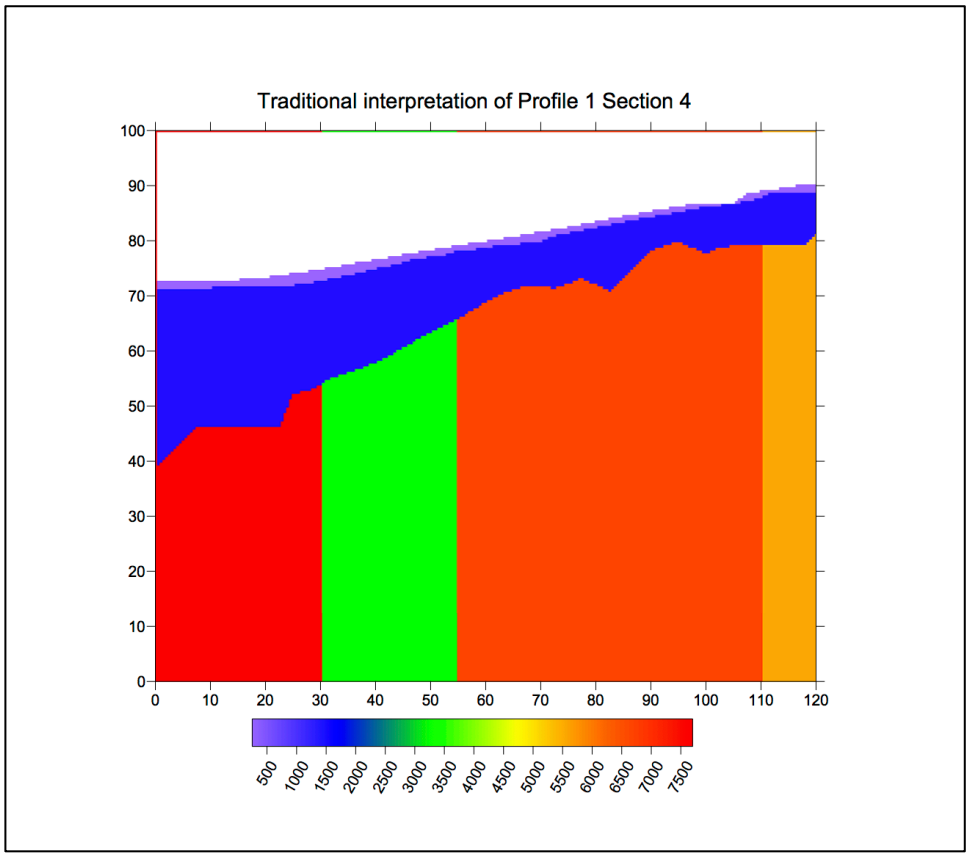

Figure 20: Traditional interpretation start model for Profile 1 Section 4.

Figure 20 is the traditional interpretation of Profile 1 Section 4. In this start model there are three distinctive layers. The first layer is thin, with velocity around 500 m/s. The second layer reaches the greatest depths to the left, down to 40 m vertically, and shallows towards the right ending at 80 m vertically. In the third layer there is a distinctive low velocity zone between 30 and 55 m, where the velocity is 3200 m/s. The interpreted velocity in the section is rather high, 6700 m/s as a maximum. This causes an illusion that there is a low velocity zone between 110 to 120 m horizontally where the velocity is 5500 m/s, and by no means a low velocity zone.

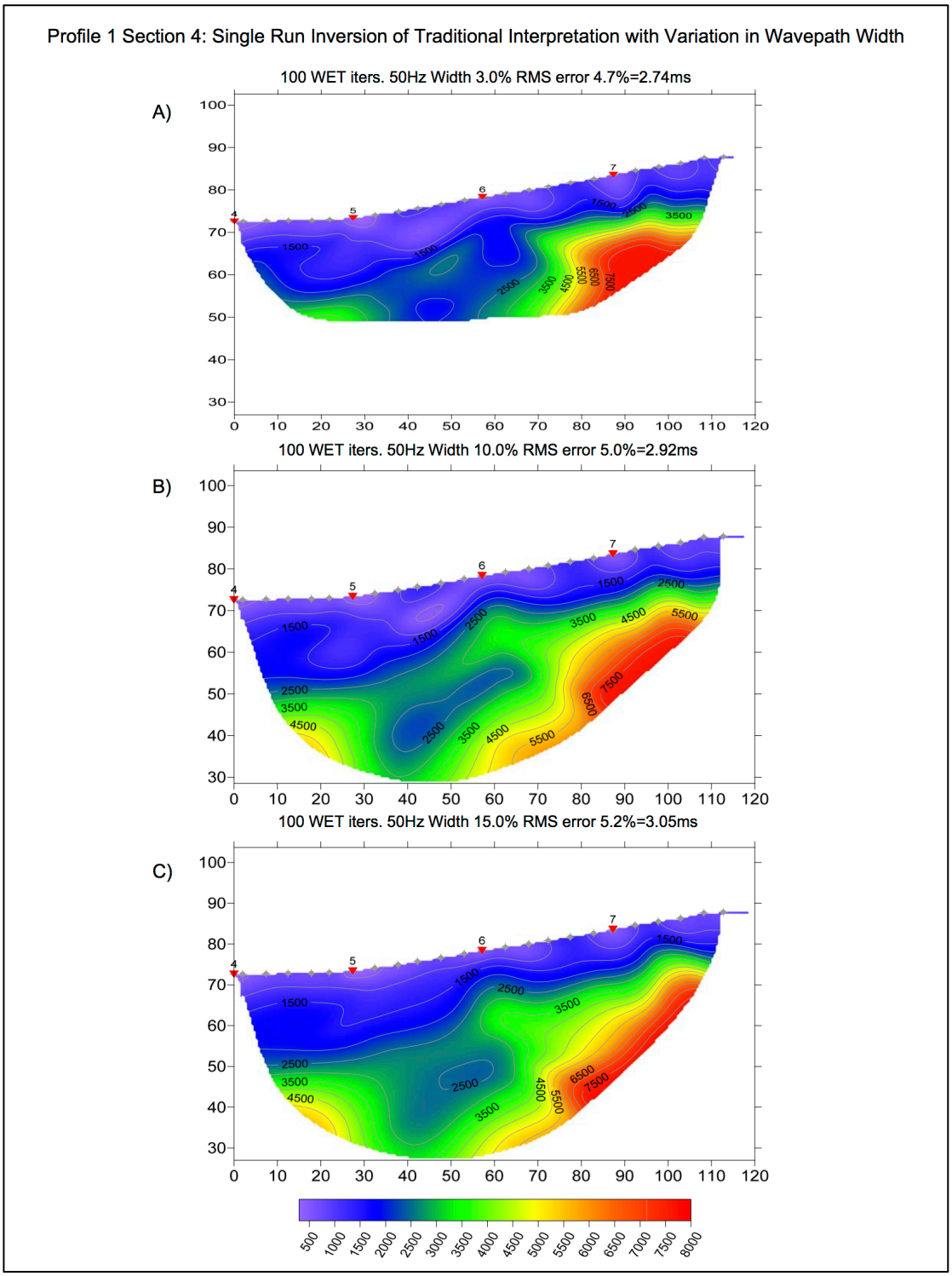

Figure 21: Inversions of Profile 1 Section 4 with the traditional interpretation as start model, WET single run and 50 Hz wavepath frequency. The wavepath width is 3, 10 and 15 % in A), B) and C) respectively.

The single run inversions of Profile 1 section 4 with 50Hz wavepath frequency and different wavepath widths are shown in Figure 21. The wavepath width is 3 % in Figure 21 A), 10 % in Figure 21 B) and 15 % in Figure 21 C). As in the inversions based on the Plus-Minus model, the RMS error increases with an increase in the

wavepath width. The inversion with 3 % wavepath width does not reach as deep as the inversions with 10 and 15 % width. Since the velocities in the inversions are based on the traditional interpretation start model, they have significantly higher velocity than the inversions based on the Plus-Minus start model, ranging from 500 to 8000 m/s. In Figure 21 B and Figure 21 C) low velocity is encapsulated in high velocity, which is, as stated previously, highly unlikely to represent a true image of the subsurface. In Figure 21 A) a very small trace of high velocity is encapsulated in lower velocity. When comparing the results in Figure 19 C) and Figure 21 C) the depth to the 3000 m/s contour line is approximately the same, but in the inversion based on the traditional interpretation the velocity rapidly increases with depth after this contour, while in the inversion based on the Plus-Minus start model the velocity stabilizes shortly after this contour.

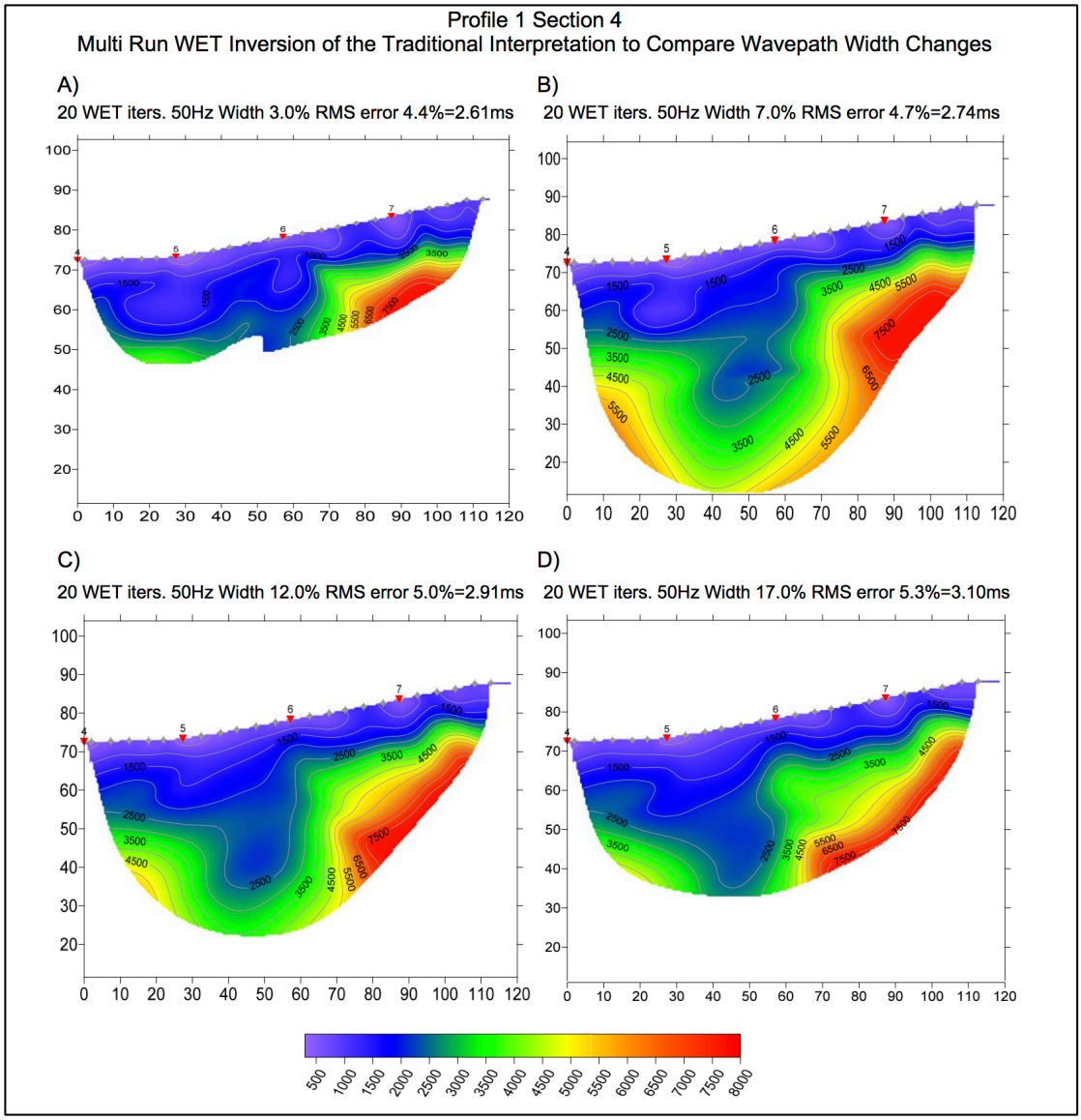

Figure 22: Inversions of Profile 1 Section 4 using the traditional interpretation as start model. Multi run inversions with 20 WET iterations and 50 Hz wavepath frequency. A) Wavepath width 30-1 %. B) Wavepath width 30-5 %. C) Wavepath width 30-10 %. D) Wavepath width 30-15 %.

Multi run inversions using the traditional interpretation as start model and 50 Hz wavepath frequency are presented in Figure 22. In Figure 22 A-D the wavepath width is 30-1, 30-5, 30-10 and 30-15 % respectively. The velocity ranges from 300 to 8000 m/s, which is significantly higher than the maximum velocity in the inversions using the same parameters but with the Plus-Minus start model. All the inversions in Figure 22 show higher velocity to the right of the section and a zone of lower velocity between the 20 and 80 m laterally. The low velocity zone is most distinctive in Figure 22 B) and C).

4.2.4 Inversions with steepest descent and conjugate gradient

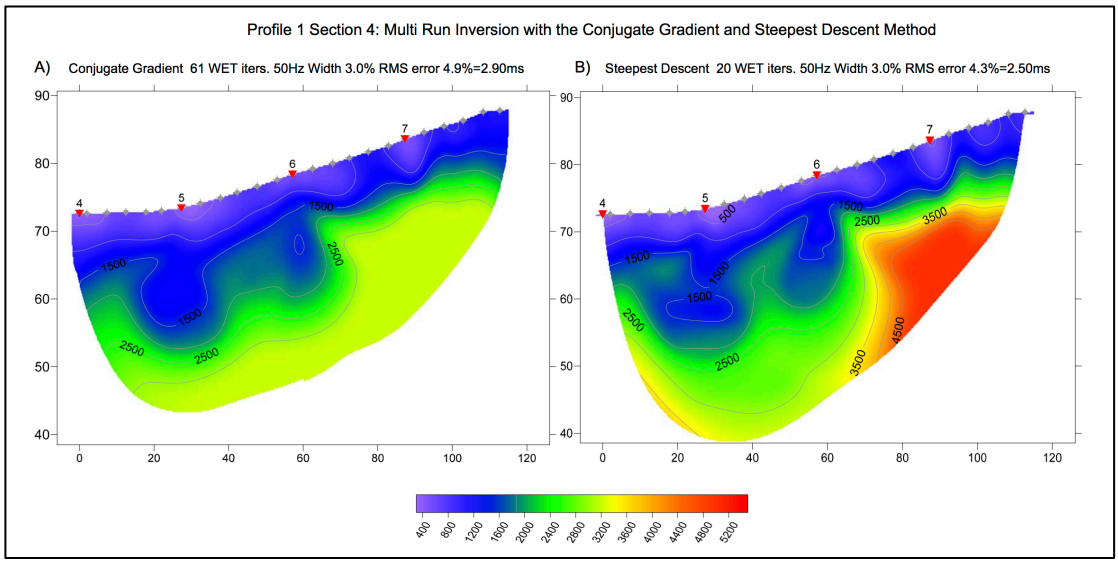

Figure 23: Profile 1 Section 4 inverted with the conjugate gradient and steepest descent method, multi run. Plus-Minus start model inverted using 50Hz wavepath frequency and 30-1 % wavepath width. A) Conjugate gradient inversion, 61 WET iterations. B) Steepest Descent inversion 20 iterations.

Figure 23 displays the inversions of Profile 1 Section 4 using the Plus-Minus start model inverted using conjugate gradient, Figure 23 A), and steepest descent, Figure 23 B). The inversion using the conjugate gradient has velocity ranging from 300 to 3000 m/s, while the inversion based on the steepest descent method have higher velocity, from 300 to 5500 m/s. Except from the difference in velocity range in the two inversion and that the steepest descent inversion reaches greater depths, the general form of the models resemble each other. The depth to the high velocity is greater in the left end of the models than in the right. In inversion using the conjugate gradient method 61 WET iterations are performed for each run, while when using the steepest descent method 20 WET inversions are performed. In the inversion using conjugate gradient method the RMS error is 4.9 %, while in the inversion using the steepest descent method the RMS error is 4.3 %.

4.2.5 Wavefront start models

Profile 1 Section 4 did not have sufficient ray coverage to create the wavefront start model. The inversions based on the wavefront start model are therefore presented for Profile 2.

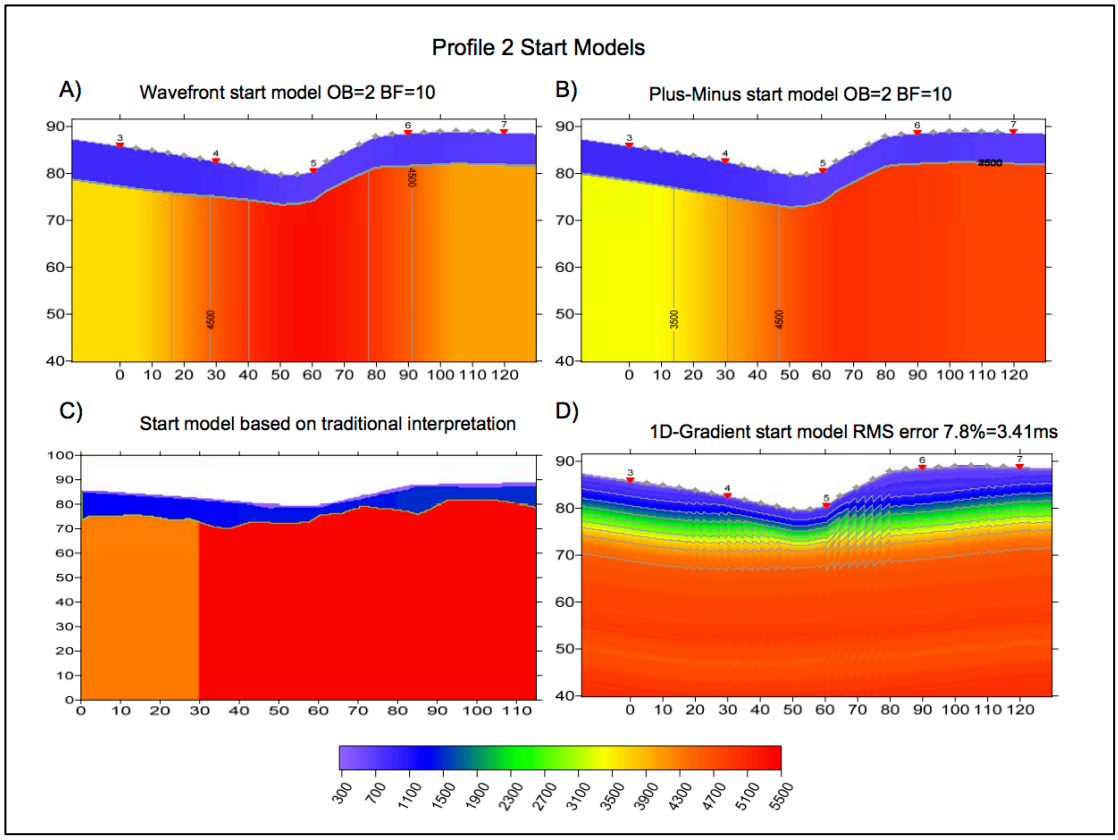

Figure 24: Start models for Profile 2. A) Wavefront start model OB= 2 BF=10. B) Plus-Minus start model, OB=2 BF=10. C) Start model based on traditional interpretation. D) 1D-Gradient start model.

The start models for Profile 2 are presented in Figure 24. Figure 24 A) and Figure 24 B) are the wavefront and the Plus-Minus start models. Both start models are two layer models. In the wavefront start model, the velocity decreases both to the left and right of the maximum velocity at the center of the profile, while the Plus-Minus start model has velocity increasing toward the right from 3500 to 4700 m/s. The traditional start model, Figure 24 C), is a three layer model with a thin layer with velocity below 400 m/s, a middle layer of velocities between 1400 and 1500 m/s. The third layer has velocity of 4400 m/s from 0 to 30 m from left and 5000 m/s from 30 to 120 m. Figure 24 D) the 1D-Gradient start model has velocity increasing with depth from 300 to 5200 m/s.

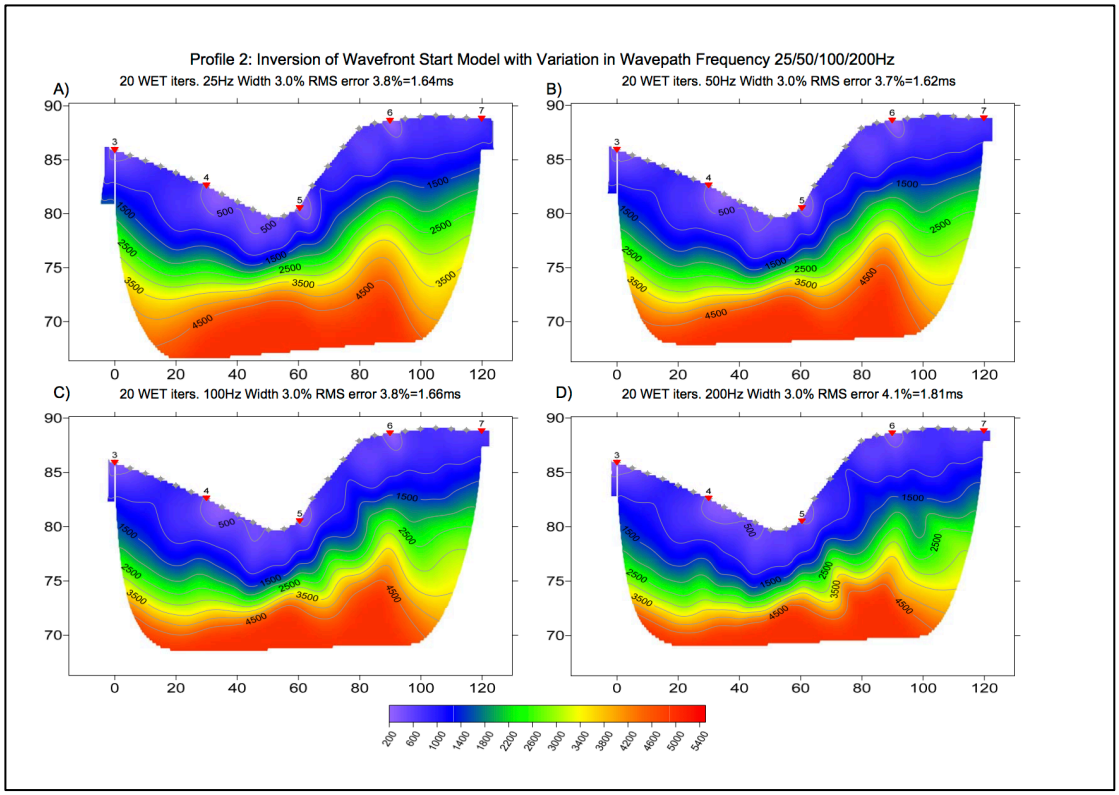

Figure 25: Multi run inversions of Profile 2 using the wavefront start model with wavepath width 30-1 %, 20 WET inversions and variations in wavepath frequency. A) Wavepath frequency 25Hz. B) Wavepath frequency 50 Hz. C) Wavepath frequency 100 Hz. D) Wavepath frequency 200 Hz.

The multi run inversions using the wavefront start model for Profile 2 with different wavepath frequencies are presented in Figure 25. The different inversions have similar form and depth to the soil bedrock interface, but the undulation of the interface varies. The velocity ranges from 200 to 5500 m/s. Figure 25 A), which represent the inversion with 25 Hz wavepath width reached the greatest depth of the four inversions, and has the least undulation in the soil bedrock interface. The RMS error of the inversion is 3.8 %. Figure 25 B), the inversion with 50Hz wavepath frequency has, by a tiny margin, the smallest RMS error, 3.7 %. The inversion with 200Hz wavepath frequency, Figure 25 D), has the shallowest reach, it approximately reaches the 70 m hash. The inversion also holds the highest RMS error of the four and has the most undulation soil bedrock contact. Figure 25 C) has slightly less undulating soil bedrock contact than Figure 25 D) and reaches marginally deeper.

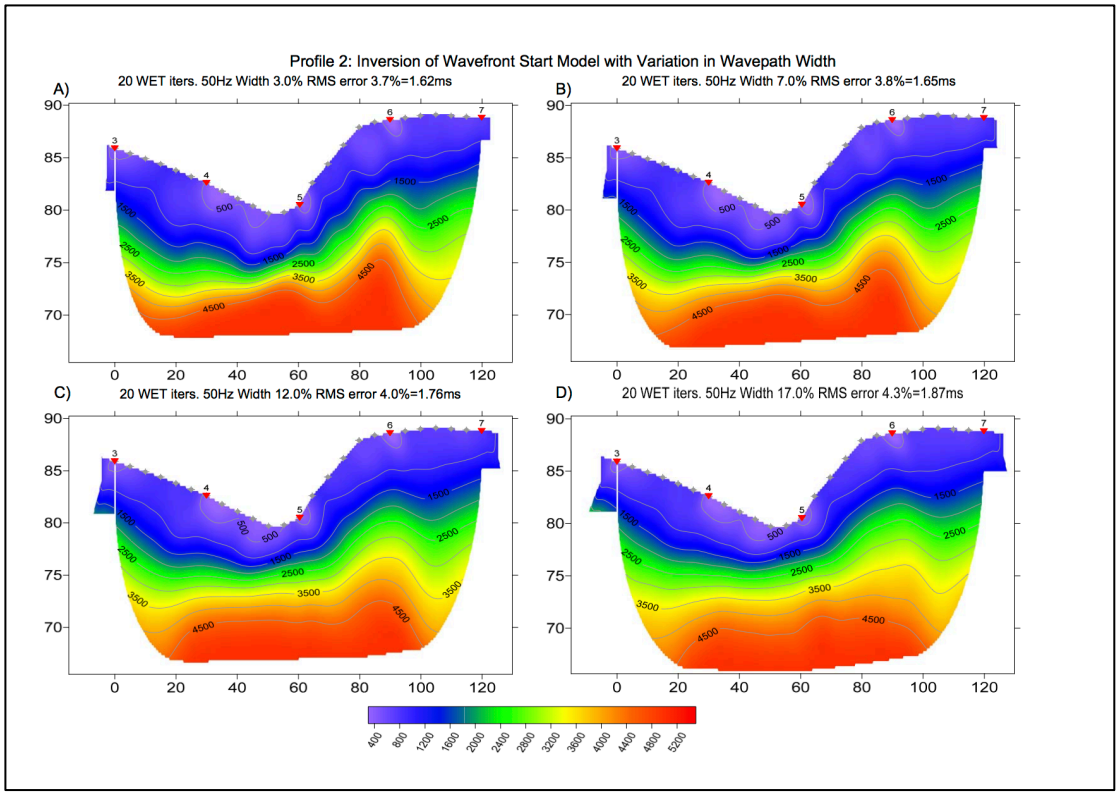

Figure 26: Multi run inversions of Profile 2 using the wavefront start model with variation in wavepath width. The wavepath frequency is set to 50Hz. A) Wavepath width 30-1 %. B) Wavepath width 30-5 %. C) Wavepeth width 30-10 %. D) Wavepath width 30-15 %.

The effect of changing the wavepath width of the multi run inversion when using the wavefront start model can be seen in Figure 26. The wavepath width is set to 30-1 % in Figure 26 A), 30-5 % in Figure 26 B), 30-10 % in Figure 26 C) and 30-15 % in Figure 26 D). The velocity ranges from 300 to 5500 m/s. As a general trend the smaller wavepath widths in Figure 26 A) and Figure 26 B) reaches shallower depths than the larger widths in Figure 26 C) and Figure 26 D). The four inversions has the same range in velocity, which causes the distance between the velocity contours to be greater in Figure 26 D) than in Figure 26 A). The RMS error of the inversion increases slightly from Figure 26 A) to Figure 26 D), which indicates that a smaller wavepath width leads to a smaller error. This coincides with the results from the inversions of the Plus-Minus and traditional interpretation start model.

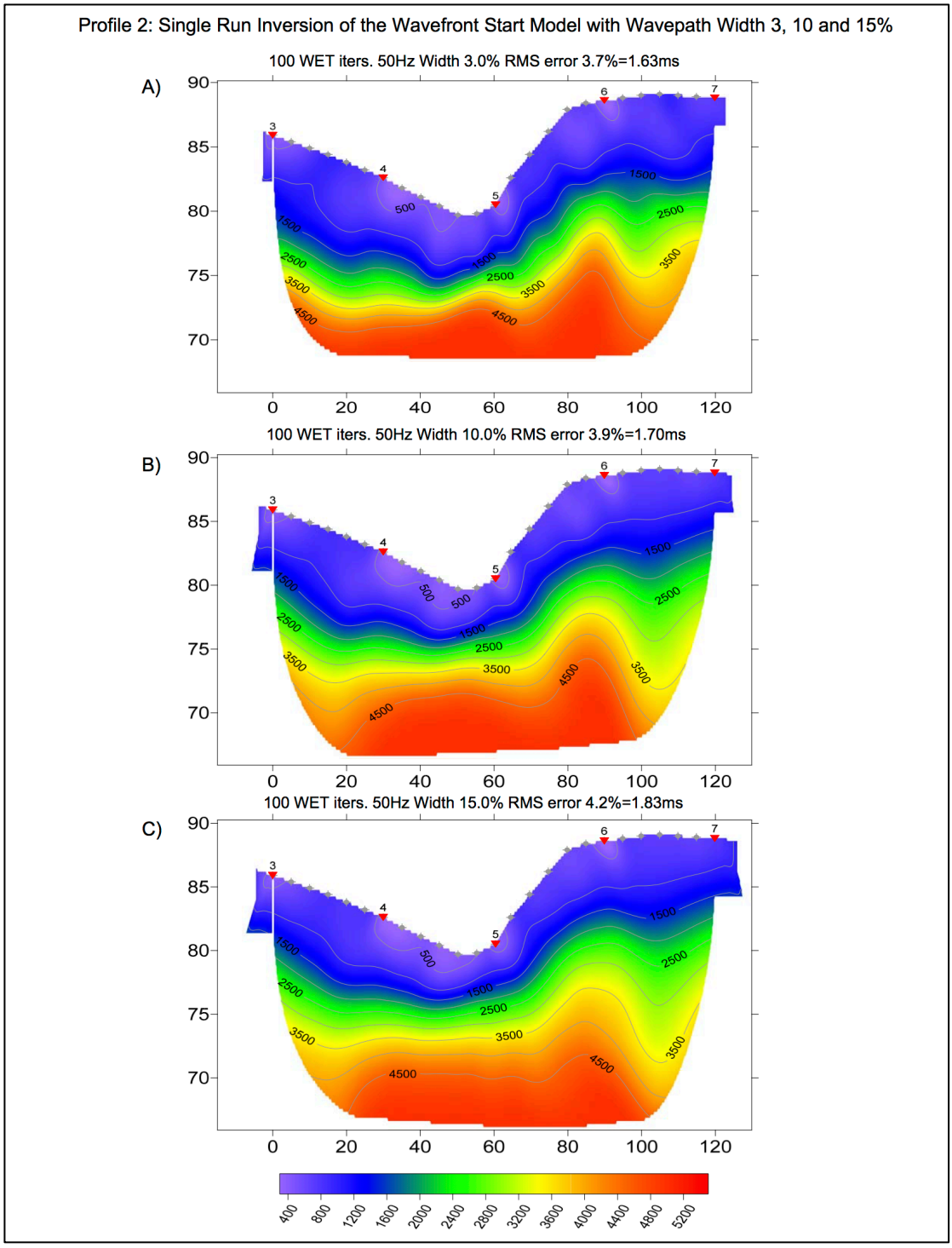

Figure 27: Single run inversion using the wavefront start model with 50 Hz wavepath frequency and 100 WET iterations. A) Wavepath width 3 %. B) Wavepath width 10 %. C) Wavepath width 15 %.

The single run inversions using the wavefront start model with different wavepath widths are presented in Figure 27. Figure 27 A) is the inversion with 3 % wavepath width, Figure 27 B) is the inversion with 10 % wavepath width and Figure 27 C) is the inversion with 15 % wavepath width. A difference in the models is the RMS error,

which increase with increasing wavepath width. Figure 27 C) reaches the greatest depth and has the highest RMS error. The undulation of the velocity contours is also increasing with the increase in wavepath width.

5. Discussion

In this section the results will be compared and discussed.

5.1 Parameters for inversion

When comparing the results in Figure 18, Figure 22 and Figure 26 where inversions run with the multi run settings on and changing wavepath width, a common feature is that the RMS error increases in the inversions where the wavepath width is broader. The inversions where the wavepath width is set to 30-1 % have lower RMS error than the inversions where the wavepath width is broader. The increase in error when the wavepath width is changed is small. The same trend, with an increase in error as the wavepath width increases, is visible in the single run inversions, Figure 19, Figure 21, and Figure 27. Due to this occurrence it can be safe to assume that the most reliable results demands a narrow wavepath width. This is in good agreement with the theory and Rayfract® manual, which states that wider wavepath width provides a smoother model.

When comparing the results from the multi run inversions using the Plus-Minus, Figure 17, and wavefront start models, Figure 25, with different wavepath frequency, the trend is that the lowest wavepath frequency yields the greatest depth. The higher velocity contours are denser in the inversions with higher wavepath frequency i.e. 200 Hz than in the ones with lower 25 Hz. The smoothness of the inversions is higher when the wavepath frequency is lower. The RMS error of the inversions is slightly lower for the inversion using 50 Hz wavepath frequency than for the inversions using higher and lower wavepath frequency.

5.2 Comparing multi and single run inversions

To decide whether the use of multi or single run inversions yields the best model of the subsurface, the corresponding inversions are compared. Comparing the inversions with the traditional interpretation used as a start model, Figure 21 A) where the single run inversion is used, and in Figure 22 A) where the multi run inversion is used, the models looks similar at first glance. A difference is the higher velocity zone

encapsulated by lower velocity at 50 m laterally in Figure 21 A). This encapsulated high velocity zone is unlikely to be a real geological event. Combining this with the fact that the multi run inversion reaches deeper into the subsurface and has a slightly lower RMS error, 4.4 % versus 4.9 %, leads to the conclusion that the multi run inversion creates the best image of the subsurface. The issue with high velocity surrounded by lower velocity in the model is also present in Figure 19 A), where Profile 1 Section 4 is inverted using single run inversion of the Plus-Minus start model. In the multi run inversion using the Plus-Minus start model, Figure 18 A), the velocity increases with depth, and there is not an encapsulated high velocity zone. In the inversions of Profile 2 based on the wavefront start model, the problem of an encapsulated high velocity zone is not present but it is noteworthy to mention that the velocity contours undulate less in the multi run inversion, Figure 26 A), than in the single run inversion, Figure 27 A).

5.3 Conjugate gradient versus steepest descent

The steepest descent inversion in Figure 23 B) has a RMS error of 4.3 %, which is lower than the RMS error of the conjugate gradient inversion of 4.9 %, Figure 23 A). The benefit of the conjugate gradient, as stated previously, should be that the technique yields a sharper image with less iteration; in this case the conjugate gradient used more iterations than the steepest descent and yields a less clear image. Combining this with the fact that the velocity of the steepest descent inversion resembles the velocity of the traditional interpretation better, leads to the conclusion that, in this survey, the steepest descent inversion is the best technique out of the two. This might be due to the fact that the steepest descent provides a more robust inversion and in this survey the shot to receiver ratio is less than ideal.

5.4 Comparing results from the seismic inversions to borehole data

Table 9: Depth to bedrock in the boreholes nearest the seismic surveys and the interpreted bedrock depth based on traditional interpretation and on Rayfract® inversions. Rayfract® multi run inversions with 50Hz wavepath frequency and 30-1 % wavepath width are used for the Plus-Minus and wavefront start models.

Section	Location (m)	Name of borehole	Distance to borehole (m)	Depth in borehole (m)	Depth in traditional interpretation (m)	Depth in Plus-Minus Inversion (m)	Depth in wavefront inversion (m)	Depth in smooth inversion (m)
Profile 2	90	TUFTE-5	84	8.4	8.2	9.5	9.5	10.2
Profile 2	120	TUFTE-6	86	7.9	9.9	N/A	N/A	N/A
Profile 1 Section 4	60	TUFTE-3	296	>18	10.5	>33	N/A	25

The locations of the boreholes are not ideal for comparing the depth to bedrock found in them to the results obtained in the seismic survey. It should be noted that performing the geophysical investigation prior to drilling, as is done in the petroleum industry, could have solved this. The depths to bedrock in the boreholes closest to the seismic surveys compared to the depths to bedrock interpreted from the seismic surveys are shown in Table 9. For Profile 1 the TUFTE-3 is the closest borehole. TUFTE-3 is 296 m northwest of the fourteenth shot of Profile 1 which corresponds to 60 m into Profile 1 Section 4. In TUFTE-3 the bedrock contact was not reached but 18 m of the drill string was used, proving that the depth to the bedrock is greater than 18 m. In the traditional interpretation the depth to bedrock 60 m into Profile 1 Section 4 was interpreted to 10.5 m, in the inversion based on the Plus-Minus start model the depth to bedrock is greater than 33 m and in the smooth inversion the depth to bedrock is 25 m.

According to the topography contours of the map in Figure 8, the elevation difference between TUFTE-3 and the 60 m shot position is approximately 15 m. The distance, both in lateral and vertical direction, from the borehole to the seismic line causes a great uncertainty in whether the depth to bedrock should be the same in the borehole as in the closest point on the seismic survey. When looking at the inversion using the Plus-Minus start model and the traditional interpretation of Profile 1 Section 4, in Figure 18 A) and Figure 20, the depth to the bedrock is greater in the right part. A theory could be that these points of great depths to the bedrock, in the borehole and along the seismic profile, are connected with a channel crossing Profile 1 from north-northwest to south-southeast.

TUFTE-5 is 84 meters south of the sixth shot of Profile 2, corresponding to 90 m along the profile. The depth to bedrock in the borehole is 8.4 m. The depth to the bedrock contact in the seismic interpretations are 8.2 m in the traditional interpretation, 9.5 m in the inversions using the Plus-Minus and wavefront start models and 10.2 m in the smooth inversion based on the 1D-Gradient start model. TUFTE-6, located 86 m north of the seventh shot of Profile 2, which is 120 m along the profile, has a measured depth to bedrock of 7.9 m. According to the traditional interpretation in the same location the depth to bedrock is 9.9 m. From the Rayfract® inversions it was not possible to interpret a depth to bedrock since the location is at

the end of the profile. This could have been resolved by planning an overlap in the survey. The correspondence of the depths to bedrock in the boreholes to the seismic interpretations of Profile 2 enhances the credibility of the interpretations.

5.5 Comparing depth in boreholes to depth in the resistivity

Table 10: Boreholes in close proximity to Profile 1, the distance to the profile and location of the projection onto the profile.

Borehole	Depth to bedrock (m)	Distance to profile (m)	Location on profile (m)
Fen MTGN58 2016	5.8	145	First point W
Fen HLA4 2016	10.8	80	270 m W
Fen HLA6 2016	15.1	214	734 from W

Information regarding the boreholes closest to resistivity profile 1 such as the measured depth to bedrock, the distance from the borehole to the profile and where the borehole is projected onto the profile are presented in Table 10. The borehole closest to profile 1 is the Fen HLA4 2016 borehole, which is located 80 m south of the profile and is projected 270 m along the profile from the starting point in the west. The depth to the bedrock in the Fen HLA4 is 10.8 m. 270 m along profile 1, Figure 25, the depth to resistivity greater than 500 Ωm is approximately 7 m, which can according to Table 1 be characterized as rock. In regards to the distance from the profile to the borehole the fit is adequate. At the first measuring point of profile 1, where Fen MTGN58 2016 is projected to, the depth to high resistivity values greater than 500 Ωm is 5 m, this corresponds well with the borehole data, even though the borehole is 145 m away.

Table 11: Boreholes in close proximity to Profile 2, the distance to the profile and location of the projection onto the profile.

Borehole	Depth to bedrock (m)	Distance to profile (m)	Location on profile (m)
Fen TEIG2 2016	6.25	33	158 from W
Fen FEN1 2016	16.2	50	250 from W
Fen SKOLE1 2016	7	138	First point to the W

The boreholes closest to resistivity profile 2, the depth to bedrock in the boreholes, the distance to the profile and where the borehole is projected onto the profile is presented in Table 11. The closest borehole is Fen TEIG2 2016, which is 33 m north of the profile. The depth in the borehole is 6.25 m; looking at Figure 26 the depth to resistivity above 500 Ωm is approximately 15 m. This can either indicate that the resistivity cannot be used to decide the depth of the bedrock in this situation, or that depth varies along the 33 m between the profile and the borehole. The theory that the depth varies in the north south direction can be supported by the fact that in the Fen FEN1 2016 borehole, which is to the northeast of the Fen TEIG2 2016 borehole and 50 m north of the profile, has a depth of 16.2 m to the bedrock. In the resistivity profile 2 the depth to the high resistivity material decrease slightly from the west to the east in the section where the boreholes are project onto the profile.

Table 12: Boreholes in close proximity to Profile 3, the distance to the profile and location of the projection onto the profile.

Borehole	Depth to bedrock (m)	Distance to profile (m)	Location on profile (m)
TUFTE-9	1	32	265 m from W
TUFTE-1	4.3	6.6	230 m form W
TUFTE-4	8.2	65	327 m from W
TUFTE-5	8.4	80	140 m from E
TUFTE-6	7.9	85	111m from E
Fen TEIG2 2016	6.25	192	Last point

The closest boreholes to the resistivity profile 3, where the boreholes are projected onto the profile and the depth to bedrock in the boreholes are listed in Table 12. When studying Figure 27 and comparing the depth to bedrock in the boreholes presented in Table 12, there is a high degree of concurrence. The TUFTE-1 borehole is the closest borehole to the profile, it is projected onto profile 3 230 m from the west of the starting point of the profile. At this point there is approximately a 5 m depth to resistivity values of 1000 Ωm, which according to the characterization in Table 1 represents fractured rock. The depth to resistivity higher than 3000 Ωm, which indicate solid rock is approximately 10 m where the boreholes TUFTE-5 and TUFTE-6 project onto the profile. This corresponds well with the depth in the boreholes being

8.4 and 7.9 m especially when considering the boreholes are 80 and 85 m away. The bedrock in TUFTE-5 and TUFTE-6 is characterized as rauhaugitt with ores of thorium present (Dahlgren, 2016). The electrical properties of the thorium ores may influence the resistivity in the area.

5.6 Comparing seismic to resistivity

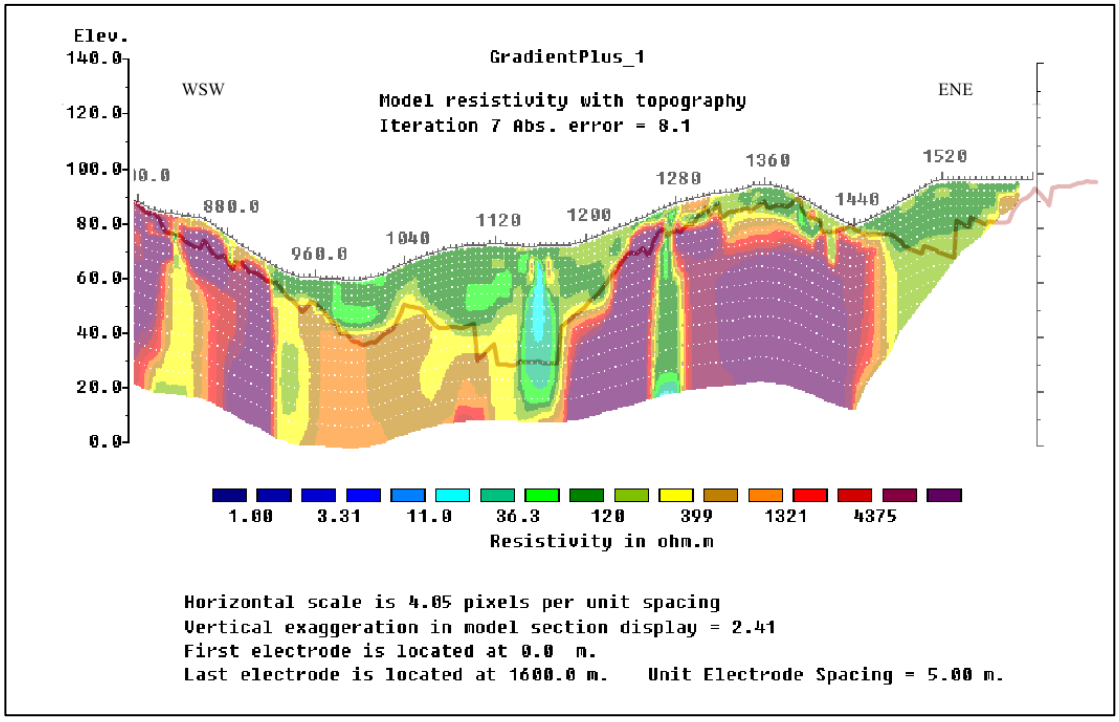

Figure 28: The depth to bedrock from the traditional seismic interpretation of seismic profile 1(red line) on top of the to the resistivity measurements corresponding section resistivity of profile 1.

In Figure 28 the depth to bedrock from the traditional interpretation of seismic profile 1 is compared to the corresponding section of resistivity profile 1. The seismic survey starts at the electrode placed at 795 m and continues 45 m past resistivity profile 1. The bedrock boundary from the traditional interpretation is presented as the red line on top of the resistivity. The correspondence between the assumed bedrock due to resistivity values and the depth to bedrock based on the traditional seismic interpretation is good.

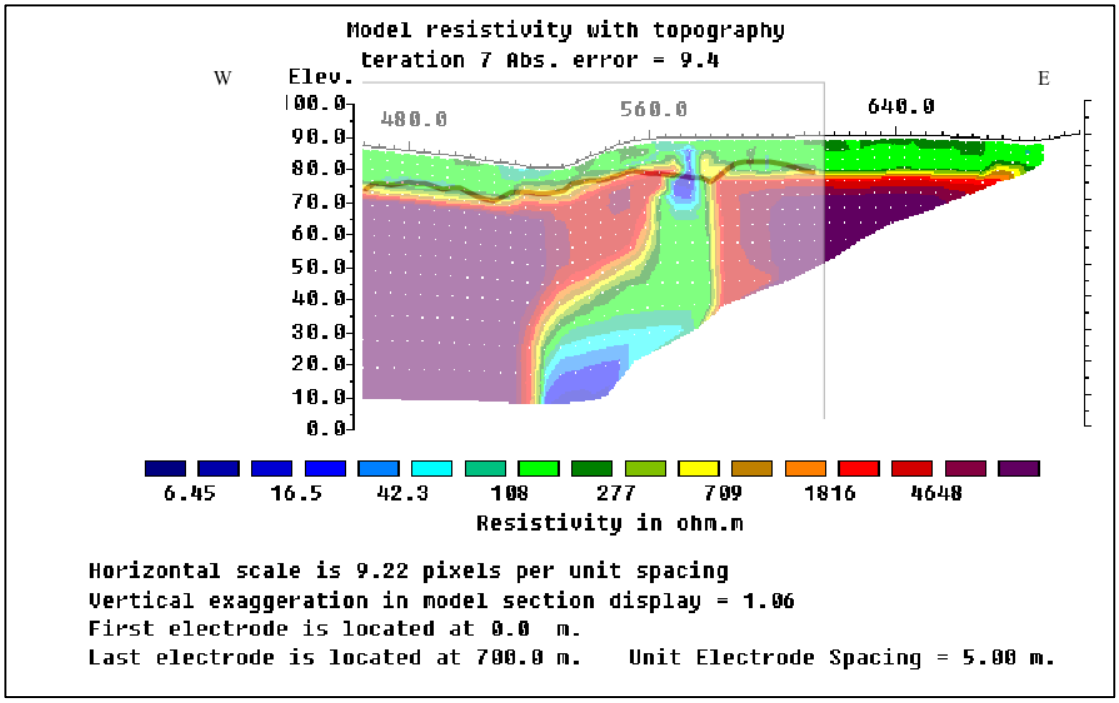

Figure 29: The depth to bedrock from traditional interpretation of seismic profile 2 (red line) on top of the corresponding section of resistivity profile 3.

Seismic profile 2 starts 470 m along resistivity profile 2 and continues to 590 m. In Figure 29 the bedrock depth from the traditional interpretation of seismic profile 2 is placed on top of the corresponding section of resistivity profile 3, the red line represents the seismic interpretation. There is a good correlation between the interpreted bedrock depth from the seismic and what would be interpreted as bedrock in the resistivity measurements. The correlation between the depths to bedrock from the traditional interpretation of the seismic to the depth to bedrock in the resistivity measurements implies that the resistivity measurements can in this study be used as an indicator for depth to bedrock.

5.7 Comparing the traditional interpretation to the interpretations from Rayfract®

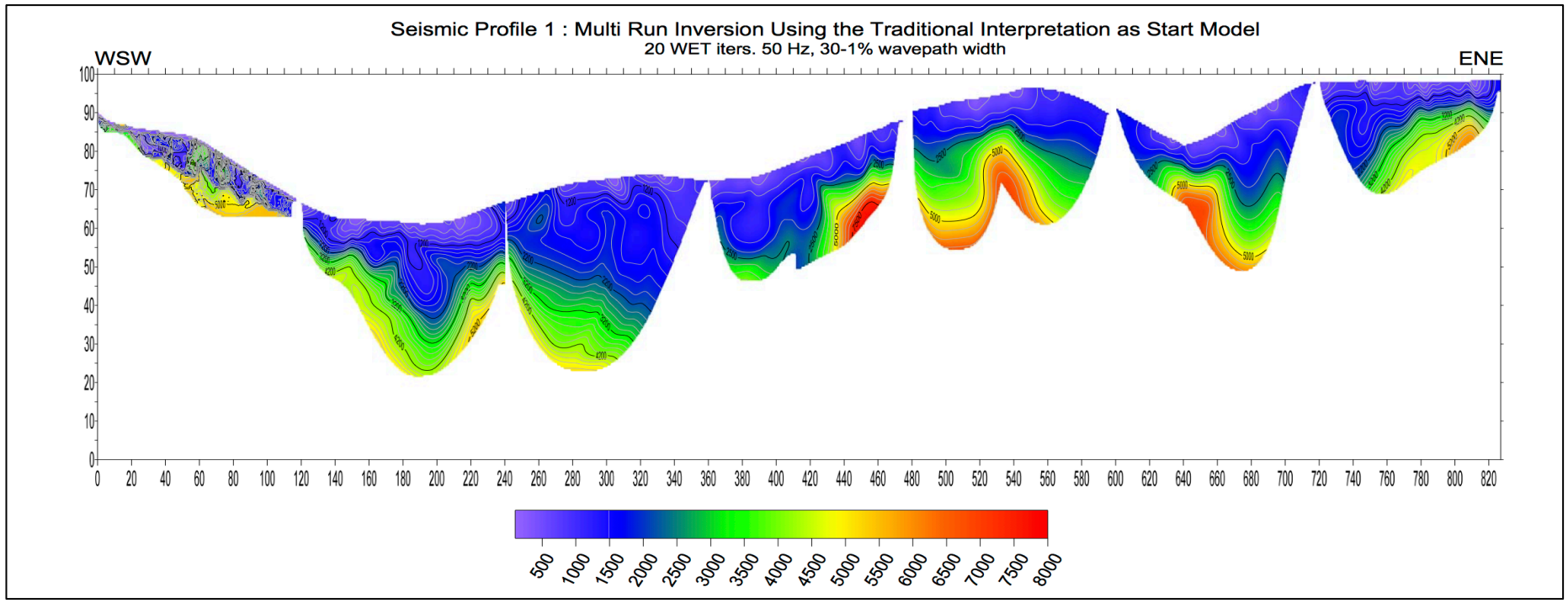

Figure 30: All WET multi run inversions of Profile 1 based on the traditional interpretation merged. The inversions have 20 iterations, 50 Hz wavepath frequency and 30-1 % wavepath width.

All sections of Profile 1 inverted with multi run inversion using the traditional start model, 20 WET iterations, 50Hz wavepath frequency and 30-1 % wavepath width are presented in Figure 30. The low velocity zones in Profile 1, their location, velocity and classification based on Figure 3 are listed in Table 13. There are in total eight low velocity zones present in the profile with classification ranging from extremely poor to poor.

Table 13: Identification of low velocity zones and classification of rock quality in the inversions based on the traditional interpretation start model of Profile 1.

Location	Velocity (m/s)	Classification based on Figure 3
180-215 m	2500-3500	Very Poor
240-250 m	2300	Extremely poor
320-360 m	2000-2500	Extremely poor
360-370 m	2500-3000	Very Poor
400-420 m	2000	Extremely poor
570-600 m	3000	Very Poor
600-620 m	2200	Extremely poor
690-740 m	2000	Extremely poor

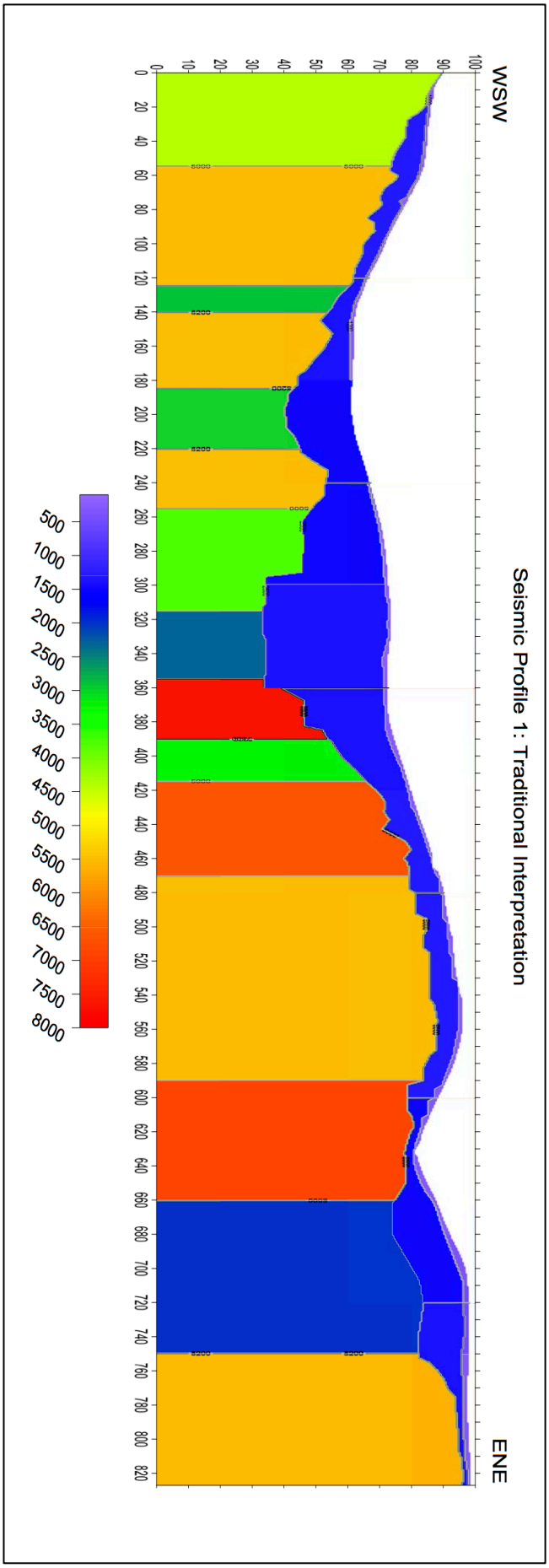

Figure 31: Traditional interpretation of all sections of Seismic Profile 1.

Figure 31 displays the traditional interpretation of all the sections of Profile 1. The zones of low velocity are tabulated in Table 14. The table provides a classification of the rock quality based on the velocity from the RQD diagram in Figure 3. In total six low velocity zones are identified in the traditional interpretation, the low velocity zones are classified as extremely poor, very poor and poor/fair.

Table 14: Identification of low velocity zones and classification of rock quality in the traditional interpretation of Profile 1

Location	Velocity (m/s)	Classification based on Figure 3
125-140 m	2900	Very Poor
185-220 m	3000	Very poor
255-315 m	2300	Extremely poor
315-355 m	2000	Extremely poor
390-415 m	3200	Very poor
660-750 m	2000	Extremely poor

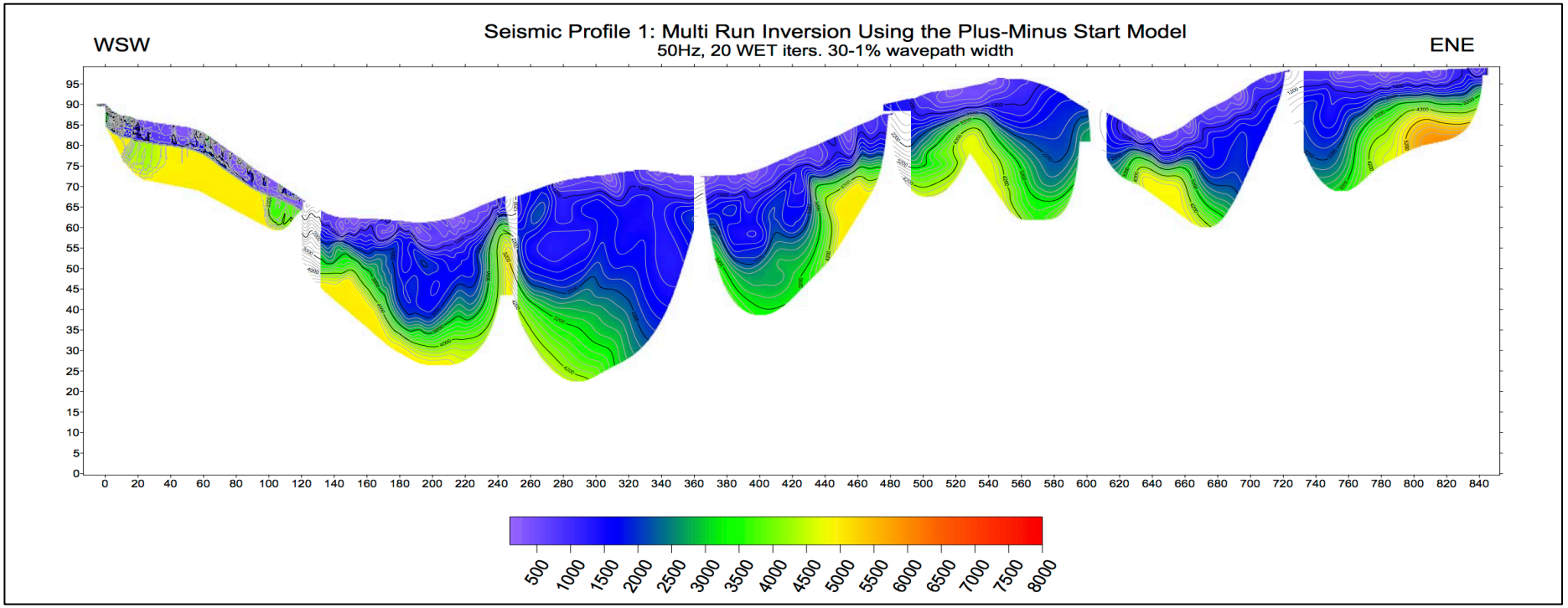

Figure 32: Inversion of all sections of Profile 1 using the Plus-Minus start and multi run settings. The inversions have 20 iterations, 50 Hz wavepath frequency and 30-1 % wavepath width.

Figure 32 displays all sections of Profile 1 inverted multi run inversion using the Plus-Minus start model with 50Hz wavepath frequency, 20 WET iterations and 30-1 % wavepath width. The low velocity zones of Profile 1 are listed with location, velocity and classification based on Figure 3 in Table 15. In total there are five low velocity zones with classification ranging from extremely poor to very poor are observed in the inversion based on the Plus-Minus start model.

Table 15: Identification of low velocity zones and classification of rock quality in the inversion of Profile 1 based on the Plus-Minus start model.

Location	Velocity (m/s)	Classification based on Figure 3
320-360 m	2000	Extremely poor
560-600 m	3000	Very poor
600-620 m	2500	Very poor
690-720 m	2000	Extremely poor
720-760 m	2500	Very poor

The low velocity zones, characterized as weakness zones, in the seismic interpretations displayed in Table 13, Table 14 and Table 15 shows that there are a different number of zones dependent on the processing of the seismic data. In the inversion using the traditional interpretation as a start model there are eight zones, in the traditional interpretation there are six zones, and in the inversion based on the Plus-Minus start model there are five zones visible. Some zones are reoccurring in the different interpretations with the same or a slightly shifted position, while other are completely unrecognizable in the other interpretations. The fact that there is such a difference in the interpretations when it comes to number, location and velocity makes it difficult to know which interpretation gives the proper model of the subsurface. Boreholes can aid in determining the validation of the interpretation, but since the boreholes at the Fen Complex are located at great distances from the seismic survey line of Profile 1, they provide little help in confirming the interpretation.

To decide which inversion is the most likely to represent the subsurface best, it is possible to look at the RMS error of the inversions. The RMS errors of the inversions are in general lower in the inversions based on the Plus-Minus start model than the inversions based on the traditional interpretation start model. This can weigh positive in the direction of choosing the inversion based on the Plus-Minus start model to be

the best interpretation of the subsurface of the two. While the traditional interpretation does not offer a RMS error, the interpretation should be within a 10 % margin of error as long as the conditions for Hagedoorn's method are valid, as stated earlier. The RMS error of the inversion based on the Plus-Minus method is smaller than 10 %. This may indicate that the best model of the subsurface is the inversion based in the Plus-Minus start model. Yet without the overlap in the receiver spreads, the inversions of the profile needs to be done in sections. When merging the sections back into a complete profile, the velocity at the end of one section is not always the same as in the beginning of the next.

5.8 Depth to bedrock based on the resistivity measurements

Along resistivity profile 1, Figure 9, from WSW to ENE, the interpreted depth to the bedrock is presented in Table 16. The depth to bedrock ranges from <1 to 25 m. In some areas the depth is not interpreted due to the resistivity values creating an image that is believed to be uncertain.

Table 16: Depth to bedrock interpreted along resistivity profile 1

Location along the profile (m)	Interpreted depth to bedrock (m)
0-120	5
120-140	<1
140-510	10
510-530	<1
530-580	12
580-650	10
640-730	7
730-910	<1
910-960	10
960-1050	20
1050-1220	25
1220-1240	15
1240-1300	N/A
1300-1430	15
1430-1600	N/A

The interpretation of depth to bedrock of resistivity profile 2, Figure 12, is presented in Table 17. The depth to the bedrock along the profile is between 7 and 20 m.

Table 17: Depth to bedrock interpreted along resistivity profile 2

Location along the profile (m)	Depth to bedrock (m)
10-65	10
65-70	20
75-86	10
85-240	15
240-290	10
290-325	15
325-350	7
350-395	10

Resistivity profile 3, Figure 13, has values that make it difficult to interpret the depth to bedrock prior to 320 m along the profile from west. Here there is lower resistivity surrounding the high resistivity, which is unlikely to be a true representation of the subsurface. After 320 m from the west the depth to resistivity in the range of 1000 Ωm, which can be interpreted as bedrock, is presented in Table 18. There are small variations in the depth to bedrock; it undulates between 7 and 10 m.

Table 18: Depth to bedrock interpreted along resistivity profile 3

Location along the profile (m)	Depth to bedrock (m)
320-345	10
345-370	7
370-395	10
395-440	7
440-515	10
515-570	7
570-695	10

5.9 Geological interpretation

Based on the results from the geophysical surveys, the information from the boreholes and the report from Regional Head Geologist, Dahlgren (2016), a geological interpretation of the area has been compiled.

According to the 'Fensfeltet - Kjerneboringer Tufte 2016' the soil in the area is dominated by marine sediments. This interpretation is not coherent with the resistivity measurements, which does not detect resistivity in the range of 1-10 Ωm, which is marine clay according to the classification by Solberg et al. in Table 2. As discussed previously, the resistivity indicates that the soil could either be dry crust clay or saturated sand and gravel. Once again the resistivity measurements and the borehole report do not correspond. According to the borehole report the drill string had to be restricted not to penetrate the soil to quickly, while Solberg (2011) claims that dry crust clay causes resistance when drilling. While drilling the sediments ascending from the borehole were classified as mud and silt, which is strikingly different from sand and gravel. One possibility is that the soil in the area is dry crust clay, which when applied water pressure for drilling changes characteristics. The resistivity values for characterizing soil are created for soil in the Trøndelag region, the properties of the soil in Telemark can be different, but it is not possible to define without further geotechnical investigation.

The comparison of the depth to bedrock in the boreholes to the depth to assumed bedrock in the resistivity profile in this study has yielded a good coherence. Due to this an interpretation of the depth to bedrock has been done along the resistivity profiles. This will be an educated guess, and can only be confirmed with absolute certainty by drilling boreholes.

According to unpublished petrophysical tests performed by NGU the density of rauhaugitt is approximately 3 g/cm^3, while the density of søvitt is approximately 2.8 g/cm^3. Applying the theory presented earlier that velocity increases with density; it can be assumed that the areas with higher velocity is more likely to be rauhaugitt than søvitt. As stated previously, the velocity in the traditional interpretations is higher than the velocity in the models inverted based on the start models created in the

Rayfract® software. In the geological interpretation the traditional interpretation is used. From Figure 31, the traditional interpretation of Profile 1, it is possible to see that in general the velocity in the section from 0 to 360 m is lower than the velocity in the section from 360 to 820 m. This may indicate that there is a change from søvitt to rauhaugitt in bedrock. The most likely place for this bedrock boundary to be located is in the low velocity zone from 315 to 355 m along Profile 1. The traditional interpretation of Profile 2, Figure 24, has bedrock velocity of 4400 and 5000 m/s. The values are more similar to the values in the areas of Profile 1 previously regarded as søvitt. This leads to the interpretation that the bedrock of Profile 2 is søvitt.

6. Further work

For the next seismic survey to be conducted at the Fen Complex an overlap in receivers in the planning of the survey can be recommended. With this overlap Rayfract® can be used to its full extend and create full profiles with better coverage. There is a newly added feature in Rayfract®, the cosine square filtering, that could be tested to investigate whether the models improve.

To create a better geological map of the Fen Complex, boreholes should be drilled in closer proximity to the geophysical surveys, and preferably after the geophysics have been interpreted. This can help support the interpretation and validate the assumptions made in the thesis. Boreholes with well logging can help characterizing the property if the different rocks, which again can be used to create a more solid geological interpretation. In regards to resolving the question of the presence of quick clay a RCPTU logging tool can be used while drilling to measure in hole resistivity.

7. Conclusion

In this thesis geophysical data, refraction seismic and resistivity data, have been acquired, processed and interpreted. The data has been used to investigate the soil characteristics, depth to bedrock, areas of possible fracture zones, and to create a geological interpretation of the area. The geophysical data has been compared with information from boreholes in regard to the depth to the bedrock and bedrock characterization. The refraction seismic has been compared to the resistivity measurements, and traditional seismic interpretation has been compared to inversions created in Rayfract®. The effect of changing the parameters in Rayfract® has been investigated.

The work has lead to the following conclusions:

- The depth to bedrock in the boreholes validates the traditional interpretation of seismic Profile 2.
- Due to the fact that there is no overlap in receiver spreads in this study, the traditional interpretation of the seismic is the best to base interpretations of the depth to bedrock on.
- The correlation between the depth to bedrock from the traditional seismic interpretation and the resistivity measurement leads to the conclusion that in this study resistivity measurements can be used to infer the depth to bedrock.
- Further geotechnical testing is necessary to conclusively classify the soil in the area.
- Using the Rayfract® software is a good alternative to traditional interpretation only if the shot coverage is sufficient and the survey is planned with an overlap in the receiver spreads.
- Inversions using the multi run setting create more precise models with less velocity inversion than single run settings.
- The best parameters for the multi run inversion are 50Hz wavepath frequency and 30-1 % wavepath width, using the Plus-Minus start model.
- For this data set, the steepest descent method creates the best inversions.

References

ALDRIDGE, D. F. & OLDENBURG, D. W. 1992. Refractor imaging using an automated wavefront reconstruction method. *Geophysics,* 57**,** 8.

BARTON, N. 2007. *Rock Quality, Seismic Velocity, Attenuation and Anisotropy,* London , UK, Taylor & Francis.

BLOM 2011. LiDAR-rapport Drangedal-Nome. Oslo: Statens Kartverk.

BRYHNI, I. & ASKHEIM, S. 2016. *Fensfeltet* [Online]. Store norske Leksikon. Available: https://snl.no/Fensfeltet [Accessed 14.11 2016].

DAHLGREN, S. 2016. Fensfeltet - Kjerneboringer Tufte 2016.

DAHLIN, T. 1993. *On the Automation of 2D Resistivity Surveying for Engineering and Environmental Applications.* Doctoral Dissertation, Lund University.

DAHLIN, T. & ZHOU, B. 2004. A numerical comparison of 2D resistivity imaging with 10 electrode arrays. *Geophysical prospection***,** 379-398.

DAHLIN, T. & ZHOU, B. 2006. Multiple-gradient array measurements for multichannel 2D resistivity imaging. *Near Surface Geophysics,* 4**,** 10.

GELLEIN, J. 2017. Geofysikk i BTV-samarbeidet. NGU.

KARTVERKET. 2007. *Norges grunnkart*. Kartverket.

KELLER, G. R. 2000. Seismic Tomography. *In:* HANCOOK, P. L. & SKINNER, B. J. (eds.) *The Oxford Companion to the Earth.* Oxford University Press.

KIM, S. 2002. 3-D eikonal solvers: First- arrival traveltimes. *Geophysics,* 67**,** 7.

LECOMTE, I., GJØYSTDAL, H., DAHLE, A. & PEDERSEN, O. C. 2000. Improving modelling and inversion in refraction seismics woth a first-order Eikonal solver. *Geophysical Prospecting,* 48**,** 17.

LOKE, M. H. 1996. *Tutorial: 2-D and 3-D electrical image surveys* [Online]. Geotomosoft solutions. [Accessed 08/02/2014.

LOKE, M. H. 2015. Rapid 2-D Resistivity &IP inversion using the least-squares method. Geotomosoft solutions.

NASUTI, A., CHAWSHIN, K., DALSEGG, E., TØNNESEN, J. F., EBBING, J. & GELLEIN, J. 2010. Electrical resistivity and refraction seismic data acquisition over a segment of the Møre-Trøndelag Fault Complec. GeologicalSurvey of Norway.

PALMER, D. 1980. The greneralized reciprocal method of seismic refractioninterpretation. *Society of Exploration Geophysicists*.

RAMBERG, I. B., BRYHNI, I. & NØTTVEDT, A. 2006. *Landet blir til Norges geologi*, Norsk Geologisk Forening.

RAWLINSON, N., POZGAY, S. & FISHWICK, S. 2010. Seimic tomography: A window into deep Earth. *Physics of the Earth and Planetary Interiors,* 178**,** 34.

REYNOLDS, J. M. 1997. *An Introduction to Applied and Environmental Geophysics,* Chichester, John Wiley & Sons Ltd.

REYNOLDS, J. M. 2011. *An Introduction to Applied and Environmental Geophysics*, Wiley-Blackwell.

ROHDEWALD, S. 2014. Optimized Interpretation of SAGEEP 2011 Blind Refraction Data with Fresnel Volume Tomography and Plus-Minus Refraction. Boston, MA USA.

ROHDEWALD, S. 2016. *Rayfract Online Help* [Online]. Intelligent Resources Inc. Available: http://www.rayfract.com.

RUHL, T. 1995. Determination of shallow refractor properties by 3D-CMP refraction seismic techniques *International Journal of Rock Mechanics and Mining Sciences &Geomechanics Abstracts,* 32**,** 1.

RØNNING, J. S., GANERØD, G. V., DALSEGG, E. & REISER, F. 2013. Resistivity mapping as a tool for identifocation and characterisation of weakness zones in crystalline bedrock: definition and testing of an interpretational model. *Bullitin of Engineering Geology and the Environment,* 73**,** 20.

RØNNING, J. S., LARSEN, B. E., ELVEBAKK, H., GAUTNEB, H., OFSTAD, F. & KNEZEVIC, J. 2017. Geophysical investigations of graphite occurrences in Bø and Øksnes municipalities, Vesterålen, Nordland County, Northern Norway 2015-2016. Trondhiem: NGU.

SOLBERG, I.-L., HANSEN, L., RØNNING, J. S. & DALSEGG, E. 2010. Veileder for bruk av resistivitetsmålinger i potensielle kvikkleireområder. Versjon 1.0. *In:* HERMANNS, R. (ed.). NGU.

SOLBERG, I.-L., RØNNING, J. S., DALSEGG, E., HANSEN, L., ROKOENGEN, K. & SANDVEN, R. 2008. Resistivity measurements as a tool for outlining quick-clay extent and vally-fill stratigraphy: a feasibility study from Buvvika, central Norway. *Canadian Geotechnical Joural,* 45**,** 15.

TELFORD, W. M., GELDART, L. P. & SHERIFF, R. E. 1990. *Applied Geophysics* Press Syndicare of the University of Cambridge.

VIDALE, J. E. 1988. Finite-Difference Calculation of Travel Times. *Bulletin of the Seismological Society of America,* 78**,** 15.